Development of a 10-year (2001–2010) 0.1-degree dataset of land-surface energy balance for mainland China

Xuelong Chen[a], Zhongbo Su[a], Yaoming Ma[b], Shaomin Liu[c], Qiang Yu[d], Ziwei Xu[c]

a Faculty of Geo-Information Science and Earth Observation, University of Twente, Enschede, The Netherlands

b Key Laboratory of Tibetan Environment Changes and Land Surface Processes, Institute of Tibetan Plateau Research, Chinese Academy of Sciences, Beijing, China

c State Key Laboratory of Remote Sensing Science, School of Geography, Beijing Normal University, Beijing, China

d Plant Functional Biology & Climate Change Cluster, University of Technology, Sydney, PO Box 123, Broadway, NSW 2007, Australia

Abstract

In the absence of high resolution estimates of the components of surface energy balance for China, we developed an algorithm based on the surface energy balance system (SEBS) to generate a dataset of land-surface energy and water fluxes on a monthly time scale from 2001 to 2010 at a 0.1 × 0.1 degree spatial resolution by using multi-satellite and meteorological forcing data. A remote-sensing-based method was developed to estimate canopy height, which was used to calculate roughness length and flux dynamics. The land-surface flux dataset was validated against "ground-truth" observations from 11 flux tower stations in China. The estimated fluxes correlate well with the stations' measurements for different vegetation types and climatic

conditions (average bias = 15.3 Wm^{-2}, RMSE = 26.4 Wm^{-2}). The quality of the data product was also assessed against the GLDAS dataset. The results show that our method is efficient for producing a high-resolution dataset of surface energy flux for the Chinese landmass from satellite data. The validation results demonstrate that more accurate downward long-wave radiation datasets are needed to be able to accurately estimate turbulent fluxes and evapotranspiration when using the surface energy balance model. Trend analysis of land-surface radiation and energy exchange fluxes revealed that the Tibetan Plateau has undergone relatively stronger climatic change than other parts of China during the last 10 years. The capability of the dataset to provide spatial and temporal information on water-cycle and land–atmosphere interactions for the Chinese landmass is examined. The product is free to download for studies of the water cycle and environmental change in China.

1. Introduction

As China is one of the fastest growing and urbanizing economies in the world, changes in land cover and land use can significantly influence the environment by altering land–atmosphere energy and water exchanges (Suh and Lee, 2004;Lin et al., 2009). For instance, rapid urban expansion has substantially changed land surface heat fluxes in the Pearl River delta (PRD) (Lin et al., 2009) and has increased sensible heat fluxes in the Beijing metropolitan area (Zhang et al., 2009a). The variability of surface energy balance and its partitioning may also have an important impact on climate variability in China (Sun and Wu, 2001). Similarly, changes in surface energy fluxes have been shown to alter the intensity of the East Asian monsoon (Zhou and Huang, 2008;Qiu, 2013;Hsu and Liu, 2003). In short, understanding variation in energy fluxes is

important for the study of climate change in China (Brauman et al., 2007). Nevertheless, the spatial and temporal variability of China's land-surface energy balance, and the magnitude of each, are still unknown.

While it is of critical importance to understand the partitioning of water and energy distribution across China's terrestrial surface, accurate monitoring of their spatial and temporal variation is notoriously difficult (Ma et al., 2011). Several field experiments are being carried out to monitor turbulent fluxes over selected land cover in China by using ground-based eddy covariance devices (Wang et al., 2010;Yu et al., 2006;Ma et al., 2008b;Li et al., 2009). However, these measurements are only representative of small areas around the locations where the measurements are being made. For this reason, establishment of an eddy-covariance flux network cannot provide a complete land-surface heat flux picture for the entire Chinese landmass.

A number of methods can be used to derive land-surface energy fluxes. Jung et al. (2009), for example, generated global spatial flux fields by using a network up-scaling method. However their flux network included only a limited number of flux stations in China. The Global Soil Wetness Project 2 (GSWP-2) (Dirmeyer et al., 2006) produced a global land surface product on a 1 × 1 degree grid for the period 1986 to 1995. The Global Land Data Assimilation System (GLDAS) (Rodell et al., 2004) can provide a global coverage in the form of 3-hourly, 0.25-degree data. Furthermore, products from the European Centre for Medium-Range Weather Forecasts (ECMWF) interim reanalysis (ERA-Interim) (Dee et al., 2011), the National Centers for Environmental Prediction (NCEP) (Kalnay et al., 1996), Modern-Era Retrospective Analysis for Research and Applications (MERRA) (Rienecker et al., 2011) and other reanalysis data can also provide temporally continuous – but coarse – spatial resolution datasets of land surface

68 fluxes. Jiménez et al. (2011) made an inter-comparison of different land-surface heat flux
69 products. When these products were applied at continental scales, the different approaches
70 resulted in large differences (Vinukollu et al., 2011a;Jiménez et al., 2011;Mueller et al., 2011).

71 The problems met by using currently available flux data in climate studies of China have been
72 reported by Zhou and Huang (2010). Zhu et al. (2012) have also reported that summer sensible
73 heat flux derived from eight datasets (including NCEP, ERA, and GLDAS) of China`s Tibetan
74 Plateau region differ from each other in their spatial distribution. In addition, all the flux datasets
75 mentioned above are based on model simulations, which have deficiencies for studying changes
76 in water-cycle and land–air interactions in China (Chen et al., 2013c;Su et al., 2013;Wang and
77 Zeng, 2012;Ma et al., 2008a).

78 A spatially and temporally explicit estimate of surface energy fluxes is of considerable interest
79 for hydrological assessments and meteorological and climatological investigations (Norman et
80 al., 2003). Satellite-sensed data of surface variables can be used to produce maps of heat and
81 water fluxes at different scales (Wang and Liang, 2008;Li et al., 2012a;Liu et al., 2010;Vinukollu
82 et al., 2011b). Remote sensing approaches to estimate surface heat and water fluxes have been
83 largely used on regional scales (Fan et al., 2007;Ma et al., 2011;Jia et al., 2012;Zhang et al.,
84 2009b;Li et al., 2012b;Shu et al., 2011), but there is no analysis of satellite-derived data currently
85 underway to produce a complete, physically-consistent, decadal land-surface heat flux dataset
86 (Jiménez et al., 2009) for the Chinese landmass. The use of remotely-sensed data offers the
87 potential of acquiring observations of variables such as albedo, land surface temperature, and
88 NDVI at a continental scale for China.

Since surface fluxes cannot be directly detected by satellite-borne sensors, an alternative for estimating continental water and energy fluxes can be derived by applying the aerodynamic theory of turbulent flux transfer (Ma et al., 2011) or by establishing statistical relationships between related satellite observations and land surface fluxes (Jiménez et al., 2009;Wang et al., 2007). Most remotely-sensed latent heat flux or evapotranspiration products have null values in urban, water, snow, barren and desert areas (Mu et al., 2007;Wang et al., 2007;Jiménez et al., 2009). This is due to the lack of a uniform representation of turbulent exchange processes over different types of land cover in their method. Meanwhile, the aerodynamic turbulent transfer method can describe the flux exchange through changes in surface roughness length over different land covers. Statistical methods establish relationships between satellite-sensed observations (e.g. *NDVI*, *LST*, albedo) and land surface fluxes through various fitting techniques (Wang et al., 2007). The simple relationships established cannot give a reasonable approximation for extreme conditions such as bare soil or other types of non-canopy land cover (e.g. lakes, deserts) because land covers behave significantly differently in land-surface energy flux partitioning. Fortunately, turbulent flux transfer parameterization can overcome the shortcomings of statistical methods and produce spatially continuous distributions of land-surface energy fluxes with prepared meteorological forcing data. For this reason we chose a more physically-based method – turbulent flux parameterization – to produce the dataset.

The challenge in using turbulent flux parameterization lies in the transition from regional to continental and global scales, because meteorological data of high resolution (i.e. 1–10 km) are not easily obtained for a large region. Recently, Chinese scientists have produced high resolution meteorological forcing data that can be used in our study. Another issue is the complexity met with the method when combining different spatial and temporal sampling input variables. This is

112 discussed in detail in Subsection 3.1. The last difficulty that has surrounded application of
113 turbulent flux parameterization at continental scales is the acquisition of roughness length. To
114 address this difficulty, we have developed a remote-sensing-based mixing technique to estimate
115 canopy heights at a continental scale and use the resulting canopy height dataset to derive, for the
116 very first time, the dynamic variation of surface roughness length for the Chinese landmass.

117 Complex topography (shown by Fig. 1) and climatic conditions in China make it very difficult to
118 obtain a clear picture of the distribution of energy and water fluxes with a high spatial resolution
119 over a relatively long period for such a large area. In our study we estimate land-surface heat
120 fluxes with energy balance and aerodynamic parameterization formulas in a revised model of the
121 surface energy balance system (SEBS) (Chen et al., 2013b;Chen et al., 2013a;Su,
122 2002;Timmermans, 2011); Previous tests show that the revised model delivers better
123 performance and improvements in cases where the type of land cover in China is bare soil, short
124 canopy or snow (Chen et al., 2013b;Chen et al., 2013a). Sensible heat flux in SEBS was derived
125 from the difference between surface temperature and air temperature by using Monin–Obukhov
126 similarity theory and bulk atmospheric boundary layer similarity (Brutsaert, 1999), which
127 parameterizes ground surface momentum and heat-transfer coefficient maps to take into account
128 surface roughness, canopy height, vegetation cover, and meteorological stability (Su et al.,
129 2001;Su, 2002;Chen et al., 2013b). The latent heat flux can then be estimated from an energy
130 balance model, assuming surface net radiation and ground flux are known (Ma et al., 2002;Allen
131 et al., 2011;Vinukollu et al., 2011b). We used high resolution reanalysis data, which merges
132 model outputs, remote sensing observations, and in-situ measurements. In addition, we also
133 assessed the accuracy of the surface energy balance terms (net radiation, sensible heat, latent heat,
134 and ground heat fluxes) and their climatic trends in the preceding decade (2001–2010).

After defining the equations of the SEBS model (Section 2), we describe (in Section 3) the input data and ground-truth measurements used in the study. Further, we assess the capacity of the remote-sensing-based product to reproduce the range and variability of measured fluxes by comparing them with in-situ flux tower measurements, followed by trend analysis of the spatial patterns of the fluxes (Section 4). Concluding remarks are found in Section 5.

2 Model description and development

The surface energy balance system model known as SEBS (Su, 2002) uses aerodynamic resistance to create a spatially coherent estimate of land surface heat fluxes. Some model inputs can be obtained from remote sensing data, while others can be obtained from meteorological forcing data (e.g. GLDAS, ERA and NCEP reanalysis data). The model's equations and the required forcing variables are described in the remainder of this section.

The surface energy balance equation can be expressed as:

$$Rn = G_0 + H + LE, \quad (1)$$

where Rn is the net radiation flux; G_0 is the ground heat flux, which is parameterized by its relationship with Rn (Su et al., 2001); H is the sensible heat flux; and LE is the latent heat flux. LE is computed by using the evaporative fraction after deriving the other three variables in Equation 1 and taking into consideration energy and water limits (Su, 2002). As these fluxes were produced with a monthly average temporal resolution, energy storage in vegetation is not considered.

156 Net radiation flux is:

157 $$Rn = (1 - \alpha) \times SWD + LWD - LWU, \quad (2)$$

158 where α is broadband albedo; *SWD* is downward surface short-wave radiation; and *LWD* and *LWU*
159 are downward and upward surface long-wave radiation, respectively.

160 Here satellite observed albedo is used. *LWU* is derived from land surface temperature (*LST*) using
161 the Stefan–Boltzmann law. Land surface emissivity is derived as described in Chen et al. (2013a).
162 *LWD* and *SWD* values are obtained from meteorological forcing data.

163

164 Sensible heat flux (*H*) is computed according to the Monin–Obukhov similarity theory (MOST):

165 $$H = k\, u_* \rho C_p (\theta_0 - \theta_a)[\ln\left(\frac{z-d}{z_{0h}}\right) - \Psi_h\left(\frac{z-d}{L}\right) + \Psi_h\left(\frac{z_{0h}}{L}\right)]^{-1}, \quad (3)$$

166 where k is the von Karman constant; u_* is friction velocity; ρ is air density; C_p is specific heat for
167 moist air; θ_0 is the potential temperature at the ground surface; θ_a is the potential air temperature
168 at height z; d is the zero plane displacement height; Ψ_h is the stability correction function for
169 sensible heat transfer (Brutsaert, 1999); and L is the Obukhov length. In our study θ_a was obtained
170 from meteorological forcing data and θ_0 was derived from Moderate Resolution Imaging
171 Spectroradiometer (MODIS) LST data. For more detailed information about u_* and the calculation
172 of L, see Su (2002) and Chen et al. (2013b).

173

174 The roughness height for heat transfer (z_{0h}) in Equation 3 is calculated as follows:

175 $$z_{0h} = \frac{z_{0m}}{\exp(kB^{-1})}. \quad (4)$$

176 Using the fractional canopy coverage, kB^{-1} at each pixel can be derived according to the
177 following modification of the equation described by Su et al. (2001):

$$kB^{-1} = {f_c}^2 \times kB_c^{-1} + {f_s}^2 \times kB_s^{-1} + 2 \times f_c \times f_s \times kB_m^{-1}, \quad (5)$$

where f_c is fractional canopy coverage and f_s is the fraction of bare soil in one pixel; kB_c^{-1} is the kB^{-1} of the canopy; kB_s^{-1} is the kB^{-1} of bare soil; and kB_m^{-1} is kB^{-1} for mixed bare soil and canopy. As kB^{-1} is the most important parameter in a MOST-based calculation of sensible heat flux, kB^{-1} has been updated by Chen et al. (2013b). The momentum roughness length used to calculate kB_s^{-1} was given a value of 0.004 (Chen et al., 2013b), and the heat roughness length of bare soil was calculated according to Yang et al. (2002). The new kB^{-1} gives a better performance than the previous version of kB^{-1} (Chen et al., 2013b;Chen et al., 2013a). Detailed evaluations of the new parameterization of kB^{-1} can be found in Chen et al. (2013b).

The roughness height for momentum transfer z_{om} in Equation 4 is derived from canopy height (HC), leaf area index (LAI) and the canopy momentum transfer model (Massman, 1997):

$$z_{om} = HC \times (1 - d/HC) \times \exp(-k \times \beta), \quad (6)$$

$$\beta = C_1 - C_2 \times \exp(-C_3 \times C_d \times LAI) \ , \quad (7)$$

where C_1 = 0.32, C_2 = 0.26, and C_3 = 15.1 are model constants related to the bulk surface drag coefficient (Massman 1997). The three constants have been tested for several canopies (Chen et al., 2013b;Cammalleri et al., 2010) and evaluated as one of the best solutions for canopy turbulent-flux parameterization (Cammalleri et al., 2010). C_d is the drag coefficient, which typically equals 0.2 (Goudriaan, 1977); d is displacement height, which is derived from HC and the wind speed extinction coefficient (Su, 2002;Su et al., 2001).

As Chen et al. (2013b) have pointed out, HC is vital for turbulent heat simulations, which makes accurate estimation of HC for the Chinese landmass important for this study. A remote-sensing-

based canopy height method (Chen et al., 2013b) was further developed to estimate canopy height distribution for the whole China in this study. Simard et al. (2011) produced a global forest canopy-height map using data from the Geoscience Laser Altimeter System (GLAS) aboard ICESat (Ice, Cloud, and land Elevation Satellite). However, short-canopy (e.g. maize, rice, wheat) height information cannot be acquired by laser techniques. Since short-canopy height usually varies by season throughout the year – crops are planted in spring and harvested in autumn – we calculated short-canopy height using an NDVI-based equation from Chen et al. (2013b):

$$HC = HC_{min} + \frac{HC_{max} - HC_{min}}{(NDVI_{max}(x,y) - NDVI_{min}(x,y))} \times (NDVI(x,y) - NDVI_{min}(x,y)) \quad (8)$$

where HC_{max} and HC_{min} are the maximum and minimum short-canopy height; HC_{min} is set to 0.0012 m (Chen et al., 2013b); and HC_{max} is set to 2.5 m, corresponding to the greatest height of seasonal crops in China. $NDVI_{min}$ and $NDVI_{max}$ are a matrix of minimum and maximum NDVI values during our 10-year study period. Each short-canopy pixel was given an $NDVI_{min}$ and $NDVI_{max}$ value to calculate the canopy height. The NDVI-based short-canopy height method above was used to fill relevant pixels with forest canopy heights of less than 10 m. Higher canopy heights (greater than 10 m) were assumed to be constant, i.e. with no seasonal change. By merging canopy heights greater than 10 m and variable short-canopy data, we constructed dynamic monthly maps of canopy heights for the Chinese landmass for the period of 2001–2010. These maps were then used to calculate land surface heat fluxes. Figure 2 gives an example of derived canopy height at 11 China flux stations.

3 Data and validation

Our modeling approach makes use of a variety of satellite-based sensor data and meteorological forcing data to estimate monthly energy and water fluxes across China. The forcing data can come from satellite-based or reanalysis datasets. Due to the influence of weather, satellite-sensed visible and thermal band data (e.g. NDVI, albedo, LST) often have spatial and temporal gaps in daily data. Various temporal and spatial gap-filling algorithms have been developed to produce continuous monthly data for satellite-sensed variables (Chen et al., 2004;Moody et al., 2005). In order to avoid both spatial and temporal gaps in the final product, we selected some specific satellite-sensed datasets for this study (see Table 1). Detailed information about each input variable is described in following subsections.

The longest period covered by the forcing dataset is approximately 31 years; the shortest is about 10 years. Spatial resolution of the dataset varies from 0.01 to 0.25 degrees and its sample frequency from 3 hours to 1 month. The meteorological forcing data developed by the Institute of Tibetan Plateau Research, Chinese Academy of Sciences (hereafter referred to as ITPCAS forcing data) (He, 2010) was constructed to study meteorological variation in China. ITPCAS forcing data covers the entire landmass of China and has the highest temporal resolution among the input datasets used. Other variables such as LST and albedo, for example, have coarser temporal resolutions (monthly) and global coverage. When combining data of different spatial and temporal resolutions, both spatial and temporal scaling issues need to be addressed.

Estimates of land-surface energy flux can be subject to large errors, due to bias in the meteorological forcing input data. The spatial distribution of meteorological variables is closely related to topography (Li et al., 2013). When interpolating meteorological input variables to finer

scales, these effects have to be accounted for (Sheffield et al., 2006), which goes beyond the scope of our study. Therefore we chose to resample the satellite product of high spatial resolution to a lower spatial resolution that matches the resolution of the meteorological input data. Also, the meteorological data were averaged to monthly values that have the same temporal resolution as the remotely-sensed input variables. ITPCAS forcing data provides us data of the highest spatial resolution among the meteorological forcing data currently available (e.g. ERA-interim, NCEP, GLDAS, MERRA). Taking into account of all these items, our aim was to produce a monthly product of 0.1 × 0.1 degree resolution land-surface heat fluxes that contains neither spatial nor temporal gaps and can be used to study seasonal and inter-annual variability in the hydrological and energy cycles of China.

3.1 Input datasets and their validations

3.1.1 Meteorological forcing data

In studies previous to ours, reanalysis data have been applied in many different ways, for example to construct land-surface forcing data (Sheffield et al., 2006), to detect climate trends (Taniguchi and Koike, 2008), and to investigate water and energy cycles at regional and continental scales (Roads and Betts, 2000). Reanalysis data has also been applied by the remote sensing community to derive estimates of global terrestrial evapotranspiration and gross primary production (Mu et al., 2007;Yuan et al., 2010). Few studies, however, have used reanalysis data together with remotely-sensed ground data to derive global land-energy fluxes (sensible heat flux, latent heat flux, net radiation, etc.).

Researchers have developed several kinds of reanalysis data. Comparisons and evaluations of these reanalysis products with in-situ observations have been performed for individual sites, specific regions, and the entire globe (Wang and Zeng, 2012;Decker et al., 2011). It is well known that inaccuracies existing in reanalysis forcing data may have substantial impacts on the simulation of land-surface energy partitioning. It is difficult to choose which reanalysis data is better for use as forcing data. Additionally, the spatial resolution of all of the above reanalysis/forcing datasets is not as high as that of remote sensing data. The ITPCAS forcing dataset was produced by merging a variety of data sources. This dataset benefits in particular from the merging of information from 740 weather stations operated by the China Meteorological Administration that have not been used in other forcing data. The dataset has already been used to run land surface models and has been shown to be more accurate than other forcing datasets (Chen et al., 2011;Liu and Xie, 2013). ITPCAS meteorological forcing data include variables such as instantaneous near-surface air temperature (Ta), near-surface air pressure (P), near-surface air specific humidity (Q), near-surface wind speed (Ws) at a temporal resolution of 3 hours, 3-hourly mean downward surface short-wave (SWD) and downward surface long-wave (LWD) radiation. The time period covered is from 1979 to 2010; the spatial resolution has a grid size of 0.1 × 0.1 degrees.

3.1.2 MODIS land surface temperature processing

MODIS (Moderate-resolution Imaging spectroradiometer) sensors have been used to produce several global and continental scale LST datasets. MOD11C3 V5 and MYD11C3 V5 products (Wan, 2009) are validated over a range of representative conditions with an average bias of less than 1 Kelvin (Coll et al., 2009;Wan and Li, 2008). The MODIS V5 monthly LST product,

MOD11C3 and MYD11C3, has a 0.05-degree grid size, without gaps and covers the period March 2000 to near present. It provides monthly daytime and night-time LST values. In our study we averaged the daytime and night-time values of MOD11C3 and MYD11C3 to represent monthly means.

After spatially interpolating the monthly mean LST from 0.05× 0.05 degree to 0.1 × 0.1 degree resolution, we picked out LST values of pixels that included the 11 flux tower stations from which in-situ measurements were gathered. The time series comparisons of LST with the ground measurements were shown by Fig. 2. It shows that the processed monthly LST can present the seasonal variations in LST over different land covers very well. The pixel values were validated against the in-situ LST measurements. Detailed information about each station is given in Subsection 3.2. The linear correlation (R = 1.0), RMSE (= 1.9 K) and MB (mean value of the satellite data minus in-situ observation = 0.5 K) indicate that the quality of the merged remotely-sensed monthly LST data in China is high. They also show that MOD11C3 V5 LST captures the in-situ LST variability of different elevations and land surfaces, which is described in Subsection 4.1.

3.1.3 Albedo

Land surface albedo determines the fraction of short-wave radiation absorbed by the ground, thus influencing the surface energy budget. Studies of land-surface energy balance require temporal and spatial albedo input data without gaps. Several research projects have been devoted to producing long-term time series of surface albedo from various satellite-borne sensors (Riihel et al., 2013;Muller et al., 2012;Liu et al., 2013a). However most of the albedo products do not

provide gap-filled time-series albedo maps. Taking MODIS MCD43B albedo product as an example, 20 to 40% of the pixels of global landmass miss valid albedo values every year (Liu et al., 2013a). Twenty percent invalid values in albedo input data will result in the same amount of empty values in output, an issue that limits albedo data that can be used in our study. After checking several albedo products (including GlobAlbedo (Muller et al., 2012), CMSAF cLouds, Albedo and RAdiation Surface Albedo (CLARA-SAL albedo) (Riihel et al., 2013), and MCD43B), we decided to use GlobAlbedo as its data does not contain spatial or temporal gaps. This albedo dataset is based on a monthly sample and has a spatial resolution of 0.05 degrees, which we interpolated to a 0.1 degree resolution for our study.

3.1.4 NDVI

The Normalized Difference Vegetation Index (NDVI) is regarded as a reliable indicator of vegetation parameters. NDVI has been widely used to explore vegetation dynamics and their relationships with environmental factors (Piao et al., 2006). NDVI data from the Systeme Pour l'Observation de la Terre (SPOT) VEGETATION sensor, distributed by Vito, have a spatial resolution of 1 km × 1 km and a temporal resolution of 10 days (synthesized on days 1, 11 and 21 of each month). In order to reduce noise resulting from clouds, the maximum NDVI value in a month for each pixel is selected to represent the canopy status of that month.

3.1.5 Canopy fraction

Canopy fraction (f_c) is defined as the fraction of ground surface covered by the vegetation canopy (varying from 0 to 1). f_c in SEBS is used to distinguish the contributions of vegetation

and soil to the roughness parameterization. Here f_c was derived from NDVI data using the following equation:

$$fc = \frac{NDVI - NDVImin}{NDVImax - NDVImin} .$$

3.2 Validation data

The product generated by our model needed to be validated by comparing it with an independent observational dataset. The energy balance measurement system (eddy covariance, four component radiation and ground heat flux) at flux sites is widely accepted as a method for direct measurement of energy and fluxes and is widely applied for assessing global evapotranspiration products (Zhang et al., 2010;Jung et al., 2011;Yan et al., 2012;Fisher et al., 2008).

To validate the product, we compiled a dataset from 11 flux stations in China with land cover types including bare soil, alpine meadow, forest, cropland, orchard, grassland, and wetlands. Elevations of these stations range from 5 m to 4800 m. The observational dataset includes data from Maqu (MQ) (Chen et al., 2013b;Wang et al., 2013), Wenjiang (WJ) (Zhang et al., 2012), Bijie (BJ) (Ma et al., 2006), Miyun (MY) (Liu et al., 2013b), Daxing (DX) (Liu et al., 2013b), Guantao (GT) (Liu et al., 2011;Liu et al., 2013b), Yucheng (YC) (Flerchinger et al., 2009), Dongtan (DT) (Zhao et al., 2009), SC (Semi-Arid Climate and Environment Observatory of Lanzhou University) (Huang et al., 2008;Wang et al., 2010;Guan et al., 2009), and Weishan (WS) stations (Lei and Yang, 2010b, a). Detailed information about each site is listed in Table 2.

Half-hourly fluxes were processed using standardized quality control procedures, which are described in the literature references for each station. The half-hourly H, LE, and four component radiation were then averaged to monthly values. Monthly average values derived

356 from less than 70% of the flux data in each month were not used in the validations. Gap filling
357 was not used for the flux measurement data.

358 # 4 Results

359 ## 4.1 Canopy height assessment

360 We checked the canopy height variations at the 10 flux station produced by equation 8 and GLAS
361 forest height (Figure 3). The derived canopy height for AL is not higher than 0.2 m, which is
362 reasonable for the local land cover. YC, GT, and WS stations located in the North China,
363 represent a typical agricultural land, where crops mature twice per year. The highest canopy
364 height is around 1.5 m, a similar magnitude to the height of maize in summer. The step decrease
365 in canopy height in June at these three stations is due to that wheat/maize is harvested and new
366 seeds are sown during this period. This step variation in the canopy height also causes similar
367 step changes in sensible and latent heat flux (shown by Fig. 5). Although the land cover near WJ
368 station is crop, it is more surround by forest in a 10 km diameter. The GLAS forest height
369 reflects this ground truth. These canopy height assessments at the observation sites enable us to
370 consider that the developed method in this work is an appropriate one for solving scarcity of
371 canopy height information at a continental area.

372 ## 4.2 Validation against flux tower measurements

373 The accuracy of remote-sensing-based land-surface heat fluxes is questionable without validation
374 against ground-based measurements (Meir and Woodward, 2010). This subsection describes the
375 validation of the SEBS model against heat flux measurements from a diverse range of climates.

376 In order to analyze the source of flux calculation errors, variables related to surface radiation
377 fluxes were all validated against flux station observations. Table 3 shows that H and LE have
378 RMSE values slightly less than 22 W/m^2, which is lower than the RMSE values of products of
379 other statistical methods (see Table 7 in (Wang et al., 2007) and Table 5 in (Jiménez et al.,
380 2009)). Indeed, Kalma et al. (2008) assessed 30 published LE validation results obtained by
381 using ground flux measurements and reported an average RMSE value of about 50 W/m^2 and
382 relative errors of 15–30%. The RMSE of our LE dataset is significantly lower than their
383 averaged RMSE value.

384 We also compared our validation results with that of other, similar products produced by a
385 previous version of SEBS. Vinukollu et al. (2011b), for instance, produced global land surface
386 fluxes with RMSE values of 40.5 W/m^2 (sensible flux) and 26.1 W/m^2 (latent flux) (calculated
387 from Table 4 in (Vinukollu et al., 2011b)), which are larger than those in our study. The
388 difference could be due to the model improvement and more accurate meteorological forcing
389 dataset used in our study. Table 3 lists the values of the statistical parameters for the validation of
390 a data product produced by GLDAS (which has the highest spatial resolution compared with
391 other available terrestrial energy-flux datasets) against the same measurements from the Chinese
392 flux stations as used in our study. According to the mean values of the statistical variables, the
393 quality of our flux dataset is comparable to GLDAS' model and data assimilation results. These
394 comparisons of accuracy demonstrate that our revised model is efficient for producing a high-
395 resolution dataset of land-surface energy fluxes for China.

396 Net radiation has relatively higher RMSE and MB values than H, LE and G_0 in the dataset
397 because its accuracy is dependent on the accuracy of the other variable estimates (albedo, LST,

SWD, LWD, LWU, etc.). Any errors in these variables can cause bias in net radiation. LWD, for example, has a linear-fitting slope value of 0.9, with most points located around the fitting line (Figure 4). The correlation coefficient is as high as 0.98, thus demonstrating that there is still room for improvement of the LWD algorithms. LWD in ITPCAS was calculated with algorithms developed from measurements from across the Tibetan Plateau. The LWD algorithms may not, therefore, be accurate for other parts of China (K. Yang, personal communication). This underlines the need for more accurate LWD radiation fluxes in order to improve the accuracy of turbulent fluxes and evapotranspiration.

In addition to the statistical evaluation of model results against observations, seasonal and inter-annual changes in the model results also need to be checked. Yucheng station, which is an agricultural experimental station with winter wheat and summer maize as dominant crops was taken as an example (Figure 5). Crops at Yucheng station mature twice per year, which is representative of warm temperate farming cropland, typical for the North China Plain. A two-year flux dataset was used to compare against values extracted from our model-derived product. The inter-annual and seasonal LST and LWU data closely match the in-situ observations. The SWD term also successfully captures seasonal variations. LWD is systematically lower than observations. The LE produced at Yucheng station not only captures seasonal variation, but also responds at step stages, which occur when the wheat is harvested or maize seeds have just been sown (from June to August). The increased sensible heat and decreased latent heat flux observed in July 2003 were caused by the wheat harvest, however this signal change is not captured by the model result. The simulated sensible and latent heat produced by SEBS has a one-month lag when compared to reality. This phenomenon is caused by adopting a maximum monthly NDVI value, resulting in faulty representation of canopy status changes in the month of June.

421 The Semi-Arid Climate and Environment Observatory of Lanzhou University (SC station) is
422 situated on China's Loess Plateau, at 1965.8 m above sea level. Annual mean precipitation there
423 is 381.1 mm and annual evapotranspiration is 1528.5 mm (Huang et al., 2008). Being typical of
424 stations operating under arid conditions, its flux measurements were compared with the grid
425 point values extracted from the model product (Figure 6). In 2008 the land surface around the
426 station was covered by snow from 19 January to 20 February. Consequently the GlobAlbedo
427 value was high for February. Unexpectedly, albedo was relatively low for January, which could
428 be caused by the coarse temporal sampling of the station pixel by the satellite sensor. The
429 calculated monthly sensible heat and latent heat in January 2008 have biases of -11.7 (with an
430 observed monthly mean sensible heat = 15 W/m^2) and -7.6 W/m^2 (with an observed monthly
431 mean latent heat = 4.8 W/m^2), respectively. The relatively large bias for SC station when
432 covered with snow may be caused by the mixed pixel around the station.

433 The results of other stations have been included in supplementary materials submitted with this
434 paper. Comparison with the results of these other stations shows that model estimates of surface
435 energy balance variables match the magnitude and seasonal variation observed at stations in
436 several contrasting ecosystems. Comparisons between the flux-tower-measured and the modeled
437 fluxes show that latent fluxes were more accurate than sensible fluxes. Comparisons with other
438 studies, which are presented in Table 4, show that the accuracy of our dataset is one of the best
439 among high-resolution datasets of land surface fluxes.

440

441 **4.3 Spatial distribution of land-surface energy fluxes.**

Using maps of average annual land-surface radiation and energy fluxes, we analyzed the spatial patterns of radiation and energy fluxes for the Chinese landmass and compared them with other products, such as GLDAS. The highest values of downward surface solar radiation (Figure 7a) are located in the southwest of the Tibetan Plateau, while the lowest values occur in the Sichuan Basin (SB). The highest levels of upward short-wave radiation (Figure 7c) occur around the snow-covered peaks of the Himalaya (HM), Karakorum (KRM) and Kunlun (KLM), and the Qilian (QLM) and Nyainqentanglha (NQM) mountain ranges. The strongest net solar radiation (SWD minus SWU) on the Chinese landmass occurs in the southern part of the Tibetan Plateau (see supplementary materials). The downward and upward long-wave radiation (Figures 7b and 7c) on the Tibetan Plateau are the lowest for the entire Chinese landmass. Southern China has the highest levels of upward and downward long-wave radiation. The highest values of net long-wave radiation (LWU minus LWD) occur in the southern and western parts of the Tibetan Plateau (see supplementary materials).

Figure 8 shows that northwestern China (NWC), the western Tibetan Plateau (TP), the inner Mongolian Plateau (MP) and the Loess Plateau (LP) have the highest yearly average values for surface sensible-heat flux. Croplands of the northern China Plain (NCP, including the lowlands of Shandong, Henan, and Hebei provinces) and the northeastern China Plain (NEP, including the lowlands of Liaoning, Jilin, and Heilongjiang provinces) have low average yearly values for sensible heat flux. The Pearl River delta (PRD) and Tarim (TRB) and Sichuan (SCB) basins also have low levels of sensible heat flux, as do the Yinchuan (YCB) and the inner Mongolian basins (IMB) along the Yellow River. This spatial distribution is consistent with GLDAS results (see supplementary materials).

464 Simulated annual latent heat fluxes (Figure 8b) exhibit a southeast to northwest decreasing
465 gradient, which is consistent with other studies (Liu et al., 2013c). The southeastern Tibetan
466 Plateau has high levels of annual latent heat flux. The Gobi desert, in the northwest of China
467 (NWC), has the lowest annual latent heat flux, followed by the western Tibetan Plateau and the
468 inner Mongolian Plateau (MP). Lake regions along the Yangtze River and the region of basins
469 along the Yellow River have relatively high levels of latent heat flux.

470 The highest levels of annual average surface net radiation (Figure 8c) can be found in
471 southwestern China and the Lhasa Basin (LB); the lowest levels occur in the Sichuan (SCB) and
472 Junggar Basins (JB). The highest levels of annual average ground-heat flux (Figure 8c) are to be
473 found in western China, due to large amounts of incoming solar radiation that occur under dry
474 conditions. The monthly average of G0 is negligible when compared with other fluxes.

475 The role of plateau heating on Asia's monsoons is being discussed vigorously (Qiu, 2013;Wu et
476 al., 2012;Boos and Kuang, 2010). Figure 9 shows seasonal comparisons of H between boreal
477 winter (DJF), spring (MAM), summer (JJA) and autumn (SON). The largest area of positive
478 sensible heating occurs in spring. Lee et al. (2011) have shown that contrasting sensible heat
479 fluxes between the Chinese landmass and the seas surrounding it during the pre-monsoon period
480 (April-May) affect monsoon development in East Asia. Figure 9 (a) shows that sources of
481 sensible heating in spring occur over the Tibetan and several other plateaus in China. During
482 summer, the highest sensible heat fluxes are to be found on the western Tibetan Plateau, the
483 eastern Loess Plateau (LP) and in northwestern China (NWC).

484 LE in summer has the largest area of high latent heating, followed by that in spring, autumn and
485 winter (Figure 10). Latent heat in summer is highest in southeastern and southern China as a

result of abundant rainfall in these regions. Similarly on irrigated land, such as that found in Yinchuan (YB), the inner Mongolian basin (IMB) and the downstream basins of the Tianshan (TM) and Kunlun (KLM) mountains, latent heat and evapotranspiration are high due to the ample supply of water in summer. Latent heat fluxes in autumn and winter are significantly lower than those of the other two seasons. The magnitudes and spatial patterns of LE in China of our product are generally consistent with other reports (Yao et al., 2013;Mu et al., 2007;Jung et al., 2010).

Net radiation in summer has the highest values of the four seasons. Most of the Chinese landmass acts as a source of surface energy for the atmosphere (Figure 11).

4.4 Trend analysis

The ability to capture the inter- and intra-annual variation for each land-surface energy variable is of interest to researchers of monsoon phenomena and climate change (Zhu et al., 2012). Indeed, understanding these variations is essential for studies on climate change and water-resource-related issues. We have calculated annual average values for each flux variable. The nonparametric Mann-Kendall test (MK) is one of the most widely used methods for hydro-meteorological time series analysis (Liu et al., 2013d;Gan, 1998). The MK method was applied to the series of annual average fluxes to check variations during the period 2001–2010. The resulting slope indicates that downward surface short-wave radiation increased during that decade over the majority of the Tibetan Plateau (Figure 12).

506 The ground solar measurements at China Meteorological Administration (CMA) stations during
507 2003–2006, as shown in Figure 1b of Yang et al. (2012), confirms the increasing trend of
508 downward surface short-wave radiation found in our study. The annual mean visibility measured
509 at these stations also displays an increasing trend (Figure 2a of Yang et al. (2012)), while ERA-
510 40 reanalyzed precipitable-water and station-observed specific humidity show a decreasing trend
511 from 2000 to 2006 (Figure3a of Yang et al. (2012)). These results indicate that the atmosphere
512 over the plateau is becoming drier, which would explain why SWD has increased during the
513 decade.

514 The upward short-wave radiation over the Himalaya (HM), the Ganges (GM), the Karakorum
515 (KRM), and the Qilian (QLM) and Nyainqentanglha (NQM) mountain ranges has also increased
516 over the last 10 years, which may be caused by the glacial retreat that has occurred in these areas
517 (Scherler et al., 2011;Yao et al., 2004). Lhasa basin (LB) has the steepest rising trend in LWU,
518 perhaps because of the relatively greater degree of anthropogenic (e.g. urbanization) activity
519 occurring in this area. The trend analysis did not reveal any clear spatial pattern in downward
520 long-wave radiation. Net radiation over several high mountain ranges (including the Himalaya,
521 the Ganges, the Karakorum and the Qilian and Nyainqentanglha mountain ranges) increased by
522 approximately 5 W/m^2 between 2001 and 2010 (Figure 13). The strongest increase in net
523 radiation occurred in the central part of the Tibetan Plateau. As Matthew (2010) has pointed out,
524 soil moisture in the central Tibetan Plateau showed an increasing trend from 1987 to 2008.
525 Wetter soil can cause the ground surface to absorb more net radiation and thus increase latent
526 heat flux. Moreover, wetter soil can increase soil heating capacity (Guan et al., 2009) and so
527 further increase ground heat flux. The increases in net radiation and soil moisture may also
528 explain a rising trend in latent heat in the central Tibetan Plateau. Clearly, the plateau is

529 experiencing accelerated environmental changes (Zhong et al., 2011;Salama et al., 2012). Indeed,
530 land-surface radiation and energy trend analyses also show that the Tibetan Plateau is
531 experiencing a relatively stronger change in land-surface radiation (verified by Tang et al. (2011)
532 and energy exchange than other parts of China.

533

534 **5 Conclusions and discussion**

535 In view of China`s highly fragmented landscape, high-resolution land-surface heat flux maps are
536 necessary for hydrological studies. As China includes arid, semi-arid, humid, and semi-humid
537 regions, quantifying its water and energy budgets is a challenge. We have developed the surface
538 energy balance system (SEBS) further to produce a land-surface heat flux dataset at a continental
539 scale of higher resolution than datasets derived using other methods.Generally, the global surface
540 energy flux data sets, including reanalysis data, do not have enough spatial and temporal
541 resolution when looking at the national-level fluxes. The surface flux data sets from reanalysis
542 data sets still contain large uncertainty, partly due to the deficiency in their land surface process
543 model that simulate land surface temperature by solving soil thermal transport equations (Chen
544 et al., 1996) and usually result in a large error in LST simulation (Chen et al., 2011;Wang et al.,
545 2014) if the model is not properly calibrated by measurements (Hogue et al., 2005). So the
546 hypothesis tested in this paper is if it is possible to neglect the complex process in the soil by
547 using satellite observed land surface temperature directly to calculate the land surface fluxes at
548 continental scale? This study has demonstrated a benchmark on how to use satellite to derive a
549 land surface flux dataset for a continental area on a personal laptop which is absolutely not
550 feasible for the land surface process modeler to do in such a time and resource economic way.

We have overcome the shortages of previous remotely-sensed evapotranspiration products which have null values in barren and desert areas. We also found a solution on how to produce a dynamic surface roughness length due to variations in the canopy height, which is closer to the reality, for a continental area. Usually, the surface roughness length is given a fixed value in numerical models. In summary, using remote sensing data and surface meteorological information, an independent data product of monthly resolution has been developed for land-surface heat flux analysis. We have validated our remote-sensing-based approach with in-situ observations from 11 flux stations in China. Taking into account the limitations of available spatial data and computing resources, we applied the model to the entire Chinese landmass using a 0.1-degree resolution meteorological dataset, MODIS LST, vegetation indices and other variables to generate a climatological dataset of land-surface energy balance for a 10-year period. The modeling results for both pixel-point and spatial distribution demonstrate that this approach meets our aims in terms of (a) being robust across a variety of land cover and climate types and (b) performing well for the temporal and spatial scales of interest. The spatial distribution maps generated for each variable of surface energy balance give important background information on the terrestrial hydrology and energy cycles. This product also demonstrates the impact of topography and climatic conditions on land–air energy and moisture exchanges in China.

The applicability of remote-sensing-based estimates of land surface fluxes is hampered by limited temporal coverage of satellite sensors (Ryu et al., 2012). Remote sensing data are snapshots of the land surface status at a particular point in space and time (Ryu et al., 2011). It is challenging to compare remote-sensing-based monthly flux data with ground measurements that are made on time scales ranging from half-hourly through to monthly. The accuracy of land surface heat fluxes is largely dependent on the remotely sensed land surface temperature. Here

574 we have made an assumption that the averaged Aqua and Terra sensors sensed LST in each
575 month can represent the monthly average LST. Terra satellite sensor passes twice a day (at about
576 10:30am, and 22:30pm local time), also the Aqua satellite passes twice a day (at about 01:30am,
577 and 13:30pm local time). So MODIS have four samples each day. The samples may not be
578 enough for calculating the monthly LST, also due to the cloud noise. Besides, the time period of
579 MODIS datasets is not longer than 15 years which may limit application of our dataset in climate
580 analysis. Additionally, the sensible heat flux over forest is underestimated by present turbulent
581 flux parameterization method in SEBS which does not take the roughness sublayer over high
582 canopy (Bosveld, 1999) into consideration.

583 The energy flux product we have developed has a spatial resolution of approximately 10 km,
584 while flux towers have a footprint of tens to hundreds of meters. The tower footprint may not be
585 representative of the larger pixel of the product, and this mismatch will result in errors if the
586 mean of the satellite pixel is different from that of the flux tower footprint. Remote-sensing-
587 based studies stress that direct comparison is a challenge because scale mismatch (Norman et al.,
588 2003) and heterogeneity of the land surface reduce the spatial representativeness of ground-site
589 measurements (Mi et al., 2006). Another challenge is validating the grid-box-based simulation
590 results on the scale of the Chinese landmass, since reliable observations of flux data are only
591 available from a few sites in the simulated region.

592 Potential effects of changes in land surface heat fluxes on the monsoon over East Asia (Lee et al.,
593 2011) as a result of China's recent urbanization can be studied further using our product. As an
594 independent satellite-based product, it can also be used as a data source for evaluating land
595 surface models. We also produced an evapotranspiration product for China land area using the

596 dataset in this paper. The land surface fluxes and evapotranspiration product can be downloaded
597 from the URL. Recent result will be shared when the forcing dataset is available:

598 https://drive.google.com/folderview?id=0B7yGrB1U9eDec2JFbnA5eldlVHc&usp=sharing

599

600 **Acknowledgements**

601 This study was supported by the Chinese National Key Program for Developing Basic Sciences
602 (2010CB951701), the Chinese National Natural Science Foundation (41275010), CAS-KNAW
603 joint PhD project, the ESA WACMOS project and the FP7 CORE-CLIMAX project. The forcing
604 dataset used in our study was developed at the Data Assimilation and Modeling Center for
605 Tibetan Multi-spheres, Institute of Tibetan Plateau Research, Chinese Academy of Sciences. We
606 thank Professor Yang Kun for his comments during the writing of this paper. For our study we
607 used eddy covariance data acquired from the scientific community and networks. We
608 acknowledge Wenjiang, Ali, Yucheng, and Weishan stations,
609 Nagqu Station of Plateau Climate and Environment, Magqu Zoige Plateau Wetlands Ecosystem
610 Research Station, and the Semi-Arid Climate and Environment Observatory of Lanzhou
611 University for providing their in-situ measurement datasets. We also acknowledge Professor
612 Xiangde Xu (CMA), Dr. Lide Tian (ITP, CAS), Dr. Yu Zhang (CAREERI, CAS), Dr. Shouhua
613 Xu (IGSNNR, CAS), Dr. Bin Zhao (Fudan University), and Dr. Huimin Lei (Tsinghua University)
614 for providing us with their flux datasets. Special thanks to the edtor, Dr. Nobuko Saigusa, for her
615 kind help during the collection of Chinaflux network dataset.

616

617 **References**

618 Allen, R., Irmak, A., Trezza, R., Hendrickx, J. M. H., Bastiaanssen, W., and Kjaersgaard, J.:
619 Satellite-based ET estimation in agriculture using SEBAL and METRIC, Hydrol Process, 25,
620 4011-4027, 10.1002/hyp.8408, 2011.

621 Boos, W. R., and Kuang, Z.: Dominant control of the South Asian monsoon by orographic
622 insulation versus plateau heating, Nature, 463, 218-222, 10.1038/nature08707, 2010.

623 Bosveld, F. C.: Exchange processes between a coniferous forest and the atmosphere, Ph.D,
624 Wageningen University, 181 pp., 1999.

625 Brauman, K., Daily, G., Duarte, T., and Mooney, H.: The nature and value of ecosystem services:
626 An overview highlighting hydrologic services, in: Annual Review of Environment and
627 Resources, Annual Review of Environment and Resources, Annual Reviews, Palo Alto, 67-98,
628 2007.

629 Brutsaert, W.: Aspects of bulk atmospheric boundary layer similarity under free-convective
630 conditions, Rev. Geophys., 37, 439-451, 10.1029/1999rg900013, 1999.

631 Cammalleri, C., Anderson, M. C., Ciraolo, G., D'Urso, G., Kustas, W. P., La Loggia, G., and
632 Minacapilli, M.: The impact of in-canopy wind profile formulations on heat flux estimation in an
633 open orchard using the remote sensing-based two-source model, Hydrol. Earth Syst. Sci., 14,
634 2643-2659, 10.5194/hess-14-2643-2010, 2010.

635 Chen, F., Mitchell, K., Schaake, J., Xue, Y., Pan, H.-L., Koren, V., Duan, Q. Y., Ek, M., and
636 Betts, A.: Modeling of land surface evaporation by four schemes and comparison with FIFE
637 observations, Journal of Geophysical Research: Atmospheres, 101, 7251-7268,
638 10.1029/95jd02165, 1996.

639 Chen, J., Jönsson, P., Tamura, M., Gu, Z., Matsushita, B., and Eklundh, L.: A simple method for
640 reconstructing a high-quality NDVI time-series data set based on the Savitzky–Golay filter,
641 Remote Sensing of Environment, 91, 332-344, http://dx.doi.org/10.1016/j.rse.2004.03.014, 2004.
642 Chen, X., Su, Z., Ma, Y., Yang, K., and Wang, B.: Estimation of surface energy fluxes under
643 complex terrain of Mt. Qomolangma over the Tibetan Plateau, Hydrol. Earth Syst. Sci., 17,
644 1607-1618, 10.5194/hess-17-1607-2013, 2013a.
645 Chen, X., Su, Z., Ma, Y., Yang, K., Wen, J., and Zhang, Y.: An Improvement of Roughness
646 Height Parameterization of the Surface Energy Balance System (SEBS) over the Tibetan Plateau,
647 J. Appl. Meteorol. Climatol., 52, 607-622, 10.1175/jamc-d-12-056.1, 2013b.
648 Chen, Y., Yang, K., He, J., Qin, J., Shi, J., Du, J., and He, Q.: Improving land surface
649 temperature modeling for dry land of China, J. Geophys. Res., 116, D20104,
650 10.1029/2011jd015921, 2011.
651 Chen, Y., Yang, K., Qin, J., Zhao, L., Tang, W., and Han, M.: Evaluation of AMSR-E retrievals
652 and GLDAS simulations against observations of a soil moisture network on the central Tibetan
653 Plateau, Journal of Geophysical Research: Atmospheres, 118, 4466-4475, 10.1002/jgrd.50301,
654 2013c.
655 Coll, C., Wan, Z., and Galve, J. M.: Temperature-based and radiance-based validations of the V5
656 MODIS land surface temperature product, J. Geophys. Res., 114, D20102,
657 10.1029/2009jd012038, 2009.
658 Decker, M., Brunke, M. A., Wang, Z., Sakaguchi, K., Zeng, X., and Bosilovich, M. G.:
659 Evaluation of the Reanalysis Products from GSFC, NCEP, and ECMWF Using Flux Tower
660 Observations, Journal of Climate, 25, 1916-1944, 10.1175/jcli-d-11-00004.1, 2011.

661 Dee, D. P., Uppala, S. M., Simmons, A. J., Berrisford, P., Poli, P., Kobayashi, S., Andrae, U.,
662 Balmaseda, M. A., Balsamo, G., Bauer, P., Bechtold, P., Beljaars, A. C. M., van de Berg, L.,
663 Bidlot, J., Bormann, N., Delsol, C., Dragani, R., Fuentes, M., Geer, A. J., Haimberger, L., Healy,
664 S. B., Hersbach, H., Hólm, E. V., Isaksen, L., Kållberg, P., Köhler, M., Matricardi, M., McNally,
665 A. P., Monge-Sanz, B. M., Morcrette, J. J., Park, B. K., Peubey, C., de Rosnay, P., Tavolato, C.,
666 Thépaut, J. N., and Vitart, F.: The ERA-Interim reanalysis: configuration and performance of the
667 data assimilation system, Quarterly Journal of the Royal Meteorological Society, 137, 553-597,
668 10.1002/qj.828, 2011.
669 Dirmeyer, P. A., Gao, X., Zhao, M., Guo, Z., Oki, T., and Hanasaki, N.: GSWP-2: Multimodel
670 Analysis and Implications for Our Perception of the Land Surface, Bulletin of the American
671 Meteorological Society, 87, 1381-1397, 10.1175/bams-87-10-1381, 2006.
672 Fan, L., Liu, S., Bernhofer, C., Liu, H., and Berger, F. H.: Regional land surface energy fluxes by
673 satellite remote sensing in the Upper Xilin River Watershed (Inner Mongolia, China),
674 Theoretical and Applied Climatology, 88, 231-245, 10.1007/s00704-006-0241-9, 2007.
675 Fisher, J. B., Tu, K. P., and Baldocchi, D. D.: Global estimates of the land–atmosphere water
676 flux based on monthly AVHRR and ISLSCP-II data, validated at 16 FLUXNET sites, Remote
677 Sensing of Environment, 112, 901-919, http://dx.doi.org/10.1016/j.rse.2007.06.025, 2008.
678 Flerchinger, G., Xaio, W., Marks, D., Sauer, T., and Yu, Q.: Comparison of algorithms for
679 incoming atmospheric long-wave radiation, Water Resour. Res., 45, W03423,
680 10.1029/2008wr007394, 2009.
681 Gan, T. Y.: Hydroclimatic trends and possible climatic warming in the Canadian Prairies, Water
682 Resources Research, 34, 3009-3015, 10.1029/98wr01265, 1998.

683 Goudriaan, J.: Crop micrometeorology: a simulation study, PhD thesis, Wageningen University
684 249 pp., 1977.
685 Guan, X., Huang, J., Guo, N., Bi, J., and Wang, G.: Variability of soil moisture and its
686 relationship with surface albedo and soil thermal parameters over the Loess Plateau, Advances in
687 Atmospheric Sciences, 26, 692-700, 10.1007/s00376-009-8198-0, 2009.
688 He, J.: Development of surface meteorological dataset of China with high temporal and spatial
689 resolution, M.S, Inst. of Tibetan Plateau Res., Chin. Acad. of Sci., Beijing, China, 2010.
690 Hogue, T. S., Bastidas, L., Gupta, H., Sorooshian, S., Mitchell, K., and Emmerich, W.:
691 Evaluation and Transferability of the Noah Land Surface Model in Semiarid Environments,
692 Journal of Hydrometeorology, 6, 68-84, 10.1175/jhm-402.1, 2005.
693 Hsu, H.-H., and Liu, X.: Relationship between the Tibetan Plateau heating and East Asian
694 summer monsoon rainfall, Geophys. Res. Lett., 30, 2066, 10.1029/2003gl017909, 2003.
695 Huang, J., Zhang, W., Zuo, J., Bi, J., Shi, J., Wang, X., Chang, Z., Huang, Z., Yang, S., Zhang,
696 B., Wang, G., Feng, G., Yuan, J., Zhang, L., Zuo, H., Wang, S., Fu, C., and Jifan, C.: An
697 overview of the semi-arid climate and environment research observatory over the Loess Plateau,
698 Adv. Atmos. Sci., 25, 906-921, 2008.
699 Jia, Z., Liu, S., Xu, Z., Chen, Y., and Zhu, M.: Validation of remotely sensed evapotranspiration
700 over the Hai River Basin, China, J. Geophys. Res., 117, D13113, 10.1029/2011jd017037, 2012.
701 Jiménez, C., Prigent, C., and Aires, F.: Toward an estimation of global land surface heat fluxes
702 from multisatellite observations, J. Geophys. Res., 114, D06305, 10.1029/2008jd011392, 2009.
703 Jiménez, C., Prigent, C., Mueller, B., Seneviratne, S. I., McCabe, M. F., Wood, E. F., Rossow, W.
704 B., Balsamo, G., Betts, A. K., Dirmeyer, P. A., Fisher, J. B., Jung, M., Kanamitsu, M., Reichle,
705 R. H., Reichstein, M., Rodell, M., Sheffield, J., Tu, K., and Wang, K.: Global intercomparison of

706 12 land surface heat flux estimates, J. Geophys. Res., 116, D02102, 10.1029/2010jd014545,
707 2011.
708 Jung, M., Reichstein, M., and Bondeau, A.: Towards global empirical upscaling of FLUXNET
709 eddy covariance observations: validation of a model tree ensemble approach using a biosphere
710 model, Biogeosciences, 6, 2001-2013, 10.5194/bg-6-2001-2009, 2009.
711 Jung, M., Reichstein, M., Ciais, P., Seneviratne, S. I., Sheffield, J., Goulden, M. L., Bonan, G.,
712 Cescatti, A., Chen, J., de Jeu, R., Dolman, A. J., Eugster, W., Gerten, D., Gianelle, D., Gobron,
713 N., Heinke, J., Kimball, J., Law, B. E., Montagnani, L., Mu, Q., Mueller, B., Oleson, K., Papale,
714 D., Richardson, A. D., Roupsard, O., Running, S., Tomelleri, E., Viovy, N., Weber, U., Williams,
715 C., Wood, E., Zaehle, S., and Zhang, K.: Recent decline in the global land evapotranspiration
716 trend due to limited moisture supply, Nature, 467, 951-954,
717 http://www.nature.com/nature/journal/v467/n7318/abs/nature09396.html#supplementary-
718 information, 2010.
719 Jung, M., Reichstein, M., Margolis, H. A., Cescatti, A., Richardson, A. D., Arain, M. A., Arneth,
720 A., Bernhofer, C., Bonal, D., Chen, J., Gianelle, D., Gobron, N., Kiely, G., Kutsch, W., Lasslop,
721 G., Law, B. E., Lindroth, A., Merbold, L., Montagnani, L., Moors, E. J., Papale, D., Sottocornola,
722 M., Vaccari, F., and Williams, C.: Global patterns of land-atmosphere fluxes of carbon dioxide,
723 latent heat, and sensible heat derived from eddy covariance, satellite, and meteorological
724 observations, J. Geophys. Res., 116, G00J07, 10.1029/2010jg001566, 2011.
725 Kalma, J., McVicar, T., and McCabe, M.: Estimating land surface evaporation: a review of
726 methods using remotely sensed surface temperature data, Surveys in Geophysics, 29, 421-469,
727 10.1007/s10712-008-9037-z, 2008.

728 Kalnay, E., Kanamitsu, M., Kistler, R., Collins, W., Deaven, D., Gandin, L., Iredell, M., Saha, S.,
729 White, G., Woollen, J., Zhu, Y., Leetmaa, A., Reynolds, R., Chelliah, M., Ebisuzaki, W.,
730 Higgins, W., Janowiak, J., Mo, K. C., Ropelewski, C., Wang, J., Jenne, R., and Joseph, D.: The
731 NCEP/NCAR 40-year reanalysis project, Bulletin of the American Meteorological Society, 77,
732 437-471, 10.1175/1520-0477(1996)077<0437:tnyrp>2.0.co;2, 1996.
733 Lee, E., Barford, C., Kucharik, C., Felzer, B., and Foley, J.: Role of turbulent heat fluxes over
734 land in the monsoon over East Asia, International Journal of Geosciences, 2 420-431,
735 10.4236/ijg.2011.24046., 2011.
736 Lei, H., and Yang, D.: Interannual and seasonal variability in evapotranspiration and energy
737 partitioning over an irrigated cropland in the North China Plain, Agricultural and Forest
738 Meteorology, 150, 581-589, http://dx.doi.org/10.1016/j.agrformet.2010.01.022, 2010a.
739 Lei, H., and Yang, D.: Seasonal and interannual variations in carbon dioxide exchange over a
740 cropland in the North China Plain, Global Change Biology, 16, 2944-2957, 10.1111/j.1365-
741 2486.2009.02136.x, 2010b.
742 Li, X., Li, X., Li, Z., Ma, M., Wang, J., Xiao, Q., Liu, Q., Che, T., Chen, E., Yan, G., Hu, Z.,
743 Zhang, L., Chu, R., Su, P., Liu, Q., Liu, S., Wang, J., Niu, Z., Chen, Y., Jin, R., Wang, W., Ran,
744 Y., Xin, X., and Ren, H.: Watershed Allied Telemetry Experimental Research, Journal of
745 Geophysical Research: Atmospheres, 114, D22103, 10.1029/2008jd011590, 2009.
746 Li, X., Liang, S., Yuan, W., Yu, G., Cheng, X., Chen, Y., Zhao, T., Feng, J., Ma, Z., Ma, M., Liu,
747 S., Chen, J., Shao, C., Li, S., Zhang, X., Zhang, Z., Sun, G., Chen, S., Ohta, T., Varlagin, A.,
748 Miyata, A., Takagi, K., Saiqusa, N., and Kato, T.: Estimation of evapotranspiration over the
749 terrestrial ecosystems in China, Ecohydrology, 7, 139-149, 10.1002/eco.1341, 2012a.

750 Li, X., Wang, L., Chen, D., Yang, K., Xue, B., and Sun, L.: Near-surface air temperature lapse
751 rates in the mainland China during 1962–2011, Journal of Geophysical Research: Atmospheres,
752 118, 7505-7515, 10.1002/jgrd.50553, 2013.
753 Li, Z., Zheng, F.-L., and Liu, W.-Z.: Spatiotemporal characteristics of reference
754 evapotranspiration during 1961–2009 and its projected changes during 2011–2099 on the Loess
755 Plateau of China, Agricultural and Forest Meteorology, 154–155, 147-155,
756 10.1016/j.agrformet.2011.10.019, 2012b.
757 Lin, W., Zhang, L., Du, D., Yang, L., Lin, H., Zhang, Y., and Li, J.: Quantification of land
758 use/land cover changes in Pearl River Delta and its impact on regional climate in summer using
759 numerical modeling, Reg Environ Change, 9, 75-82, 10.1007/s10113-008-0057-5, 2009.
760 Liu, J., and Xie, Z.: Improving simulation of soil moisture in China using a multiple
761 meteorological forcing ensemble approach, Hydrol. Earth Syst. Sci., 17, 3355-3369,
762 10.5194/hess-17-3355-2013, 2013.
763 Liu, N., Liu, Q., Wang, L., Liang, S., Wen, J., Qu, Y., and Liu, S.: A statistics-based temporal
764 filter algorithm to map spatiotemporally continuous shortwave albedo from MODIS data, Hydrol.
765 Earth Syst. Sci., 17, 10.5194/hess-17-2121-2013, 2013a.
766 Liu, R., Wen, J., Wang, X., Wang, L., Tian, H., Zhang, T. T., Shi, X. K., Zhang, J. H., and Lv, S.
767 N.: Actual daily evapotranspiration estimated from MERIS and AATSR data over the Chinese
768 Loess Plateau, Hydrol. Earth Syst. Sci., 14, 47-58, 10.5194/hess-14-47-2010, 2010.
769 Liu, S., Xu, Z., Wang, W., Jia, Z., Zhu, M., Bai, J., and Wang, J.: A comparison of eddy-
770 covariance and large aperture scintillometer measurements with respect to the energy balance
771 closure problem, Hydrol. Earth Syst. Sci., 15, 1291-1306, 10.5194/hess-15-1291-2011, 2011.

772 Liu, S. M., Xu, Z. W., Zhu, Z. L., Jia, Z. Z., and Zhu, M. J.: Measurements of evapotranspiration
773 from eddy-covariance systems and large aperture scintillometers in the Hai River Basin, China,
774 Journal of Hydrology, 487, 24–38, 10.1016/j.jhydrol.2013.02.025,, 2013b.
775 Liu, Y., Zhou, Y., Ju, W., Chen, J., Wang, S., He, H., Wang, H., Guan, D., Zhao, F., Li, Y., and
776 Hao, Y.: Changes of evapotranspiration and water yield in China's terrestrial ecosystems during
777 the period from 2000 to 2010, Hydrol. Earth Syst. Sci., 17, 2121–2129, 10.5194/hessd-10-5397-
778 2013, 2013c.
779 Liu, Z., Zhou, P., Zhang, F., Liu, X., and Chen, G.: Spatiotemporal characteristics of
780 dryness/wetness conditions across Qinghai Province, Northwest China, Agricultural and Forest
781 Meteorology, 182-183, http://dx.doi.org/10.1016/j.agrformet.2013.05.013, 2013d.
782 Ma, L., Zhang, T., Li, Q., Frauenfeld, O. W., and Qin, D.: Evaluation of ERA-40, NCEP-1, and
783 NCEP-2 reanalysis air temperatures with ground-based measurements in China, J. Geophys. Res.,
784 113, D15115, 10.1029/2007jd009549, 2008a.
785 Ma, Y., Su, Z., Li, Z., Koike, T., and Menenti, M.: Determination of regional net radiation and
786 soil heat flux over a heterogeneous landscape of the Tibetan Plateau, Hydrological Processes, 16,
787 2963-2971, 2002.
788 Ma, Y., Zhong, L., Su, Z., Ishikawa, H., Menenti, M., and Koike, T.: Determination of regional
789 distributions and seasonal variations of land surface heat fluxes from Landsat-7 Enhanced
790 Thematic Mapper data over the central Tibetan Plateau area, J. Geophys. Res., 111, D10305,
791 10.1029/2005jd006742, 2006.
792 Ma, Y., Zhong, L., Wang, B., Ma, W., Chen, X., and Li, M.: Determination of land surface heat
793 fluxes over heterogeneous landscape of the Tibetan Plateau by using the MODIS and in situ data,
794 Atmos. Chem. Phys., 11, 10461-10469, 10.5194/acp-11-10461-2011, 2011.

795 Ma, Y., Kang, S., Zhu, L., Xu, B., Tian, L., and Yao, T.: Tibetan Observation and Research
796 Platform- Atmosphere–land interaction over a heterogeneous landscape, Bull. Amer. Meteor.
797 Soc., 89, 1487–1492, 10.1175/2008BAMS2545.1, 2008b.
798 Massman, W. J.: An analytical one-dimensional second-order closure model of turbulence
799 statistics and the lagrangian time scale within and above plant canopies of arbitrary structure,
800 Boundary Layer Meteorology, 83, 407-421, 1997.
801 Matthew, O.: Characterization of the effects of climate variation on land surface temperature and
802 soil moisture through stochastic analysis of long term SSM/I observations over the Tibetan
803 plateau, Master, International Institute for Geo-information Science and Earth Observation,
804 University of Twente, Enschede, The Netherlands, 1-67 pp., 2010.
805 Meir, P., and Woodward, F. I.: Amazonian rain forests and drought: response and vulnerability,
806 New Phytologist, 187, 553-557, 10.1111/j.1469-8137.2010.03390.x, 2010.
807 Mi, N., Yu, G. R., Wang, P. X., Wen, X. F., and Sun, X. M.: A preliminary study for spatial
808 representiveness of flux observation at ChinaFLUX sites, Science in China Series D-Earth
809 Sciences, 49, 24-35, 10.1007/s11430-006-8024-9|ISSN 1006-9313, 2006.
810 Moody, E. G., King, M. D., Platnick, S., Schaaf, C. B., and Feng, G.: Spatially complete global
811 spectral surface albedos: value-added datasets derived from Terra MODIS land products,
812 Geoscience and Remote Sensing, IEEE Transactions on, 43, 144-158, 10.1109/tgrs.2004.838359,
813 2005.
814 Mu, Q., Heinsch, F. A., Zhao, M., and Running, S. W.: Development of a global
815 evapotranspiration algorithm based on MODIS and global meteorology data, Remote Sensing of
816 Environment, 111, 519-536, 10.1016/j.rse.2007.04.015, 2007.

817 Mueller, B., Seneviratne, S. I., Jimenez, C., Corti, T., Hirschi, M., Balsamo, G., Ciais, P.,
818 Dirmeyer, P., Fisher, J. B., Guo, Z., Jung, M., Maignan, F., McCabe, M. F., Reichle, R.,
819 Reichstein, M., Rodell, M., Sheffield, J., Teuling, A. J., Wang, K., Wood, E. F., and Zhang, Y.:
820 Evaluation of global observations-based evapotranspiration datasets and IPCC AR4 simulations,
821 Geophys. Res. Lett., 38, L06402, 10.1029/2010gl046230, 2011.
822 Muller, J.-P., López, G., Watson, G., Shane, N., Kennedy, T., Yuen, P., Lewis, P., Fischer, J.,
823 Guanter, L., Domench, C., Preusker, R., North, P., Heckel, A., Danne, O., and Krämer, U.: The
824 ESA GlobAlbedo Project for mapping the Earth's land surface albedo for 15 Years from
825 European Sensors., , IEEE Geoscience and Remote Sensing Symposium (IGARSS) , IEEE, ,
826 Munich, Germany, , 2012.
827 Norman, J. M., Anderson, M. C., Kustas, W. P., French, A. N., Mecikalski, J., Torn, R., Diak, G.
828 R., Schmugge, T. J., and Tanner, B. C. W.: Remote sensing of surface energy fluxes at 101-m
829 pixel resolutions, Water Resources Research, 39, 1221, 10.1029/2002wr001775, 2003.
830 Piao, S., Mohammat, A., Fang, J., Cai, Q., and Feng, J.: NDVI-based increase in growth of
831 temperate grasslands and its responses to climate changes in China, Global Environmental
832 Change, 16, 340-348, http://dx.doi.org/10.1016/j.gloenvcha.2006.02.002, 2006.
833 Qiu, J.: Monsoon Melee, Science, 340, 1400-1401, 10.1126/science.340.6139.1400, 2013.
834 Rienecker, M. M., Suarez, M. J., Gelaro, R., Todling, R., Bacmeister, J., Liu, E., Bosilovich, M.
835 G., Schubert, S. D., Takacs, L., Kim, G.-K., Bloom, S., Chen, J., Collins, D., Conaty, A., da
836 Silva, A., Gu, W., Joiner, J., Koster, R. D., Lucchesi, R., Molod, A., Owens, T., Pawson, S.,
837 Pegion, P., Redder, C. R., Reichle, R., Robertson, F. R., Ruddick, A. G., Sienkiewicz, M., and
838 Woollen, J.: MERRA: NASA's Modern-Era Retrospective Analysis for Research and
839 Applications, Journal of Climate, 24, 3624-3648, 10.1175/jcli-d-11-00015.1, 2011.

840 Riihel, A., Manninen, T., Laine, V., Andersson, K., and Kaspar, F.: CLARA-SAL: a global 28-yr
841 timeseries of Earth's black-sky surface albedo, Atmos. Chem. Phys., 13, 3743-3762,
842 10.5194/acp-13-3743-2013, 2013.
843 Roads, J., and Betts, A.: NCEP–NCAR and ECMWF reanalysis surface water and energy
844 budgets for the Mississippi River Basin, Journal of Hydrometeorology, 1, 88-94, 10.1175/1525-
845 7541(2000)001<0088:nnaers>2.0.co;2, 2000.
846 Rodell, M., Houser, P. R., Jambor, U., Gottschalck, J., Mitchell, K., Meng, C. J., Arsenault, K.,
847 Cosgrove, B., Radakovich, J., Bosilovich, M., Entin, J. K., Walker, J. P., Lohmann, D., and Toll,
848 D.: The Global Land Data Assimilation System, Bulletin of the American Meteorological
849 Society, 85, 381-394, 10.1175/bams-85-3-381, 2004.
850 Ryu, Y., Baldocchi, D. D., Kobayashi, H., van Ingen, C., Li, J., Black, T. A., Beringer, J., van
851 Gorsel, E., Knohl, A., Law, B. E., and Roupsard, O.: Integration of MODIS land and atmosphere
852 products with a coupled-process model to estimate gross primary productivity and
853 evapotranspiration from 1 km to global scales, Global Biogeochemical Cycles, 25, GB4017,
854 10.1029/2011gb004053, 2011.
855 Ryu, Y., Baldocchi, D. D., Black, T. A., Detto, M., Law, B. E., Leuning, R., Miyata, A.,
856 Reichstein, M., Vargas, R., Ammann, C., Beringer, J., Flanagan, L. B., Gu, L., Hutley, L. B.,
857 Kim, J., McCaughey, H., Moors, E. J., Rambal, S., and Vesala, T.: On the temporal upscaling of
858 evapotranspiration from instantaneous remote sensing measurements to 8-day mean daily-sums,
859 Agricultural and Forest Meteorology, 152, 212-222,
860 http://dx.doi.org/10.1016/j.agrformet.2011.09.010, 2012.
861 Salama, M. S., Velde, R., Zhong, L., Ma, Y., Ofwono, M., and Su, Z.: Decadal variations of land
862 surface temperature anomalies observed over the Tibetan Plateau by the Special Sensor

863 Microwave Imager (SSM/I) from 1987 to 2008, Climatic Change, 114, 769-781,
864 10.1007/s10584-012-0427-3, 2012.
865 Scherler, D., Bookhagen, B., and Strecker, M. R.: Spatially variable response of Himalayan
866 glaciers to climate change affected by debris cover, Nature Geosci, 4, 156-159,
867 http://www.nature.com/ngeo/journal/v4/n3/abs/ngeo1068.html#supplementary-information,
868 2011.
869 Sheffield, J., Goteti, G., and Wood, E. F.: Development of a 50-Year high-resolution global
870 dataset of meteorological forcings for land surface modeling, Journal of Climate, 19, 3088-3111,
871 10.1175/jcli3790.1, 2006.
872 Shu, Y., Stisen, S., Jensen, K. H., and Sandholt, I.: Estimation of regional evapotranspiration
873 over the North China Plain using geostationary satellite data, International Journal of Applied
874 Earth Observation and Geoinformation, 13, 192-206, 10.1016/j.jag.2010.11.002, 2011.
875 Simard, M., Pinto, N., Fisher, J. B., and Baccini, A.: Mapping forest canopy height globally with
876 spaceborne lidar, J. Geophys. Res., 116, G04021, 10.1029/2011jg001708, 2011.
877 Su, Z., Schmugge, T., Kustas, W. P., and Massman, W. J.: An evaluation of two models for
878 estimation of the roughness height for heat transfer between the land surface and the atmosphere,
879 Journal of Applied Meteorology, 40, 1933-1951, 2001.
880 Su, Z.: The Surface Energy Balance System(SEBS) for estimation of turbulent heat fluxes,
881 Hydrology and Earth System Sciences, 6, 85-99, 2002.
882 Su, Z., de Rosnay, P., Wen, J., Wang, L., and Zeng, Y.: Evaluation of ECMWF's soil moisture
883 analyses using observations on the Tibetan Plateau, Journal of Geophysical Research:
884 Atmospheres, 118, 5304-5318, 10.1002/jgrd.50468, 2013.

885 Suh, M.-S., and Lee, D.-K.: Impacts of land use/cover changes on surface climate over east Asia
886 for extreme climate cases using RegCM2, Journal of Geophysical Research: Atmospheres, 109,
887 D02108, 10.1029/2003jd003681, 2004.
888 Sun, L., and Wu, G.: Influence of land evapotranspiration on climate variations, Science in China
889 Series D: Earth Sciences, 44, 838-846, 10.1007/bf02907096, 2001.
890 Tang, W. J., Yang, K., Qin, J., Cheng, C. C. K., and He, J.: Solar radiation trend across China in
891 recent decades: a revisit with quality-controlled data, Atmos. Chem. Phys., 11, 393-406,
892 10.5194/acp-11-393-2011, 2011.
893 Taniguchi, K., and Koike, T.: Seasonal variation of cloud activity and atmospheric profiles over
894 the eastern part of the Tibetan Plateau, J. Geophys. Res.-Atmos., 113, 10104-10104, 2008.
895 Timmermans, J.: Coupling optical and thermal directional radiative transfer to biophysical
896 processes in vegetated canopies, Phd, faculty of geo-information science and earth observation,
897 University of Twente, Enchede, The Netherlands, 1-157 pp., 2011.
898 Vinukollu, R. K., Meynadier, R., Sheffield, J., and Wood, E. F.: Multi-model, multi-sensor
899 estimates of global evapotranspiration: climatology, uncertainties and trends, Hydrol Process, 25,
900 3993-4010, 10.1002/hyp.8393, 2011a.
901 Vinukollu, R. K., Wood, E. F., Ferguson, C. R., and Fisher, J. B.: Global estimates of
902 evapotranspiration for climate studies using multi-sensor remote sensing data: Evaluation of
903 three process-based approaches, Remote Sensing of Environment, 115, 801-823,
904 10.1016/j.rse.2010.11.006, 2011b.
905 Wan, Z., and Li, Z. L.: Radiance-based validation of the V5 MODIS land-surface temperature
906 product, International Journal of Remote Sensing, 29, 5373-5395, 10.1080/01431160802036565,
907 2008.

908 Collection-5 MODIS land surface temperature products users' guide.
909 http://www.icess.ucsb.edu/modis/LstUsrGuide/usrguide.html, 2009.
910 Wang, A., and Zeng, X.: Evaluation of multireanalysis products with in situ observations over
911 the Tibetan Plateau, J. Geophys. Res., 117, D05102, 10.1029/2011jd016553, 2012.
912 Wang, A., Barlage, M., Zeng, X., and Draper, C. S.: Comparison of land skin temperature from a
913 land model, remote sensing, and in-situ measurement, Journal of Geophysical Research:
914 Atmospheres, 2013JD021026, 10.1002/2013jd021026, 2014.
915 Wang, G., Huang, J., Guo, W., Zuo, J., Wang, J., Bi, J., Huang, Z., and Shi, J.: Observation
916 analysis of land-atmosphere interactions over the Loess Plateau of northwest China, J. Geophys.
917 Res., 115, D00K17, 10.1029/2009jd013372, 2010.
918 Wang, K., Wang, P., Li, Z., Cribb, M., and Sparrow, M.: A simple method to estimate actual
919 evapotranspiration from a combination of net radiation, vegetation index, and temperature,
920 Journal of Geophysical Research: Atmospheres, 112, D15107, 10.1029/2006jd008351, 2007.
921 Wang, K., and Liang, S.: An improved method for estimating global evapotranspiration based on
922 satellite determination of surface net radiation, vegetation index, temperature, and soil moisture,
923 Journal of Hydrometeorology, 9, 712-727, 10.1175/2007jhm911.1, 2008.
924 Wang, S., Zhang, Y., Lv, S., Liu, H., and Shang, L.: Estimation of turbulent fluxes using the
925 flux-variance method over alpine meadows surface in eastern Tibetan Plateau, Advances in
926 Atmospheric Sciences, 30, 411-424, 10.1007/s00376-012-2056-1, 2013.
927 Wu, G., Liu, Y., He, B., Bao, Q., Duan, A., and Jin, F.-F.: Thermal controls on the Asian
928 summer monsoon, Sci. Rep., 2, 404, 10.1038/srep00404 (2012), 2012.
929 Yan, H., Wang, S. Q., Billesbach, D., Oechel, W., Zhang, J. H., Meyers, T., Martin, T. A.,
930 Matamala, R., Baldocchi, D., Bohrer, G., Dragoni, D., and Scott, R.: Global estimation of

931 evapotranspiration using a leaf area index-based surface energy and water balance model,
932 Remote Sensing of Environment, 124, 581-595, 10.1016/j.rse.2012.06.004, 2012.
933 Yang, K., Koike, T., Fujii, H., Tamagawa, K., and Hirose, N.: Improvement of surface flux
934 parametrizations with a turbulence-related length, Quarterly Journal of the Royal Meteorological
935 Society, 128, 2073-2087, 2002.
936 Yang, K., Ding, B., Qin, J., Tang, W., Lu, N., and Lin, C.: Can aerosol loading explain the solar
937 dimming over the Tibetan Plateau?, Geophys. Res. Lett., 39, L20710, 10.1029/2012gl053733,
938 2012.
939 Yao, T., Wang, Y., Liu, S., Pu, J., Shen, Y., and Lu, A.: Recent glacial retreat in High Asia in
940 China and its impact on water resource in Northwest China, Science in China Series D: Earth
941 Sciences, 47, 1065-1075, 10.1360/03yd0256, 2004.
942 Yao, Y., Liang, S., Cheng, J., Liu, S., Fisher, J. B., Zhang, X., Jia, K., Zhao, X., Qin, Q., Zhao,
943 B., Han, S., Zhou, G., Zhou, G., Li, Y., and Zhao, S.: MODIS-driven estimation of terrestrial
944 latent heat flux in China based on a modified Priestley–Taylor algorithm, Agricultural and Forest
945 Meteorology, 171–172, 187-202, http://dx.doi.org/10.1016/j.agrformet.2012.11.016, 2013.
946 Yu, G.-R., Wen, X.-F., Sun, X.-M., Tanner, B. D., Lee, X., and Chen, J.-Y.: Overview of
947 ChinaFLUX and evaluation of its eddy covariance measurement, Agricultural and Forest
948 Meteorology, 137, 125-137, http://dx.doi.org/10.1016/j.agrformet.2006.02.011, 2006.
949 Yuan, W., Liu, S., Yu, G., Bonnefond, J.-M., Chen, J., Davis, K., Desai, A. R., Goldstein, A. H.,
950 Gianelle, D., Rossi, F., Suyker, A. E., and Verma, S. B.: Global estimates of evapotranspiration
951 and gross primary production based on MODIS and global meteorology data, Remote Sensing of
952 Environment, 114, 1416-1431, http://dx.doi.org/10.1016/j.rse.2010.01.022, 2010.

953 Zhang, C., Chen, F., Miao, S., Li, Q., Xia, X., and Xuan, C.: Impacts of urban expansion and
954 future green planting on summer precipitation in the Beijing metropolitan area, Journal of
955 Geophysical Research: Atmospheres, 114, D02116, 10.1029/2008jd010328, 2009a.
956 Zhang, K., Kimball, J. S., Nemani, R. R., and Running, S. W.: A continuous satellite-derived
957 global record of land surface evapotranspiration from 1983 to 2006, Water Resources Research,
958 46, W09522, 10.1029/2009wr008800, 2010.
959 Zhang, L., Li, Y., Li, Y., and Zhao, X.: Seasonal changes of turbulent fluxes at a typical
960 agricultural site in the Chengdu Plain based on quality-controlled data, Journal of the
961 Meteorological Society of Japan. Ser. II, 90C, 195-202, 2012.
962 Zhang, X., Ren, Y., Yin, Z.-Y., Lin, Z., and Zheng, D.: Spatial and temporal variation patterns of
963 reference evapotranspiration across the Qinghai-Tibetan Plateau during 1971&-2004, J. Geophys.
964 Res., 114, D15105, 10.1029/2009jd011753, 2009b.
965 Zhao, B., Yan, Y., Guo, H., He, M., Gu, Y., and Li, B.: Monitoring rapid vegetation succession
966 in estuarine wetland using time series MODIS-based indicators: An application in the Yangtze
967 River Delta area, Ecological Indicators, 9, 346-356,
968 http://dx.doi.org/10.1016/j.ecolind.2008.05.009, 2009.
969 Zhong, L., Su, Z., Ma, Y., Salama, M. S., and Sobrino, J. A.: Accelerated changes of
970 environmental conditions on the Tibetan Plateau caused by climate change, Journal of Climate,
971 24, 6540-6550, 10.1175/jcli-d-10-05000.1, 2011.
972 Zhou, L., and Huang, R.: Interdecadal variability of sensible heat flux in arid and semi-arid
973 region of Northwest China and its relationship to summer precipitation in China (in Chinese),
974 Chinese J. Atmos. Sci., 32, 1276-1288, 2008.

975 Zhou, L., and Huang, R.: An assessment of the quality of surface sensible heat flux derived from
976 reanalysis data through comparison with station observations in Northwest China, Advances in
977 Atmospheric Sciences, 27, 500-512, 10.1007/s00376-009-9081-8, 2010.
978 Zhu, X., Liu, Y., and Wu, G.: An assessment of summer sensible heat flux on the Tibetan
979 Plateau from eight data sets, Science China Earth Sciences, 55, 779-786, 10.1007/s11430-012-
980 4379-2, 2012.

981

982

983

984

985

986

987

988

989

990

991

992

993

994

995 Table 1. Input datasets used for calculating land surface fluxes for China (see Sections 2 and 3
996 for an explanation of abbreviations)

Variables	Data source	Temporal resolution	Availability	Domain	Spatial resolution (degrees)	Method
SWD	ITPCAS	3 hours	1979-2010	China land	0.1	Reanalysis
SWU	ITPCAS& GlobAlbedo	3 hours	1982-2009	China land	0.1	Satellite&Reanalysis
LWD	ITPCAS	3 hours	1979-2010	China land	0.1	Reanalysis
LWU	MOD11C3& MYD11C3 V5&Emis of Chen et al. 2013	1 month	2000-2012	China land	0.05	Satellite
Ta	ITPCAS	3 hours	1979-2010	China land	0.1	Reanalysis
Q	ITPCAS	3 hours	1979-2010	China land	0.1	Reanalysis
Ws	ITPCAS	3 hours	1979-2010	China land	0.1	Reanalysis
P	ITPCAS	3 hours	1979-2010	China land	0.1	Reanalysis
LST	MOD11C3 V5& MYD11C3 V5	1 month	2000-2012	Global	0.05	Satellite
h_c	GLAS&SPOT VEGETATION	1 month	2000-2012	China land	0.01	Satellite
A	GlobAlbedo	1 month	2000-2010	Global	0.05	Satellite
NDVI	SPOT VEGETATION	10 days	1998-2012	Global	0.01	Satellite
LAI	MOD15A2& MCD15A2	8 days	Feb, 2000-Jul, 2002 Aug, 2002-2012/	Global	0.01	Satellite

997

998

999

1000

1001

1002

1003 Table 2. Flux tower sites supplying measurement data for product validation

	Lat[deg]/ Lon[deg]	Land cover	Eddy covariance	Radiometer	Measurement period	Site elevation (m)	Reference
WJ	30.4200N/ 103.5000E	Crop	CSAT3,Licor7500 (10 HZ)	CNR-1	Mar 2008 - Aug 2009	539	Zhang et al. (2012)
MQ	33.8872N/ 102.1406E	Alpine meadow	CSAT3,Licor7500 (10 HZ)	CNR-1	Apr 2009 - May 2010	3439	Wang et al. (2013)
AL	33.3905N/ 79.7035E	Bare soil	CSAT3,Licor7500 (10 HZ)	CNR-1	Jul 2010 - Dec 2010	4700	Ma et al. (2008b)
BJ	31.3686N/ 91.8986E	Alpine grass	CSAT3,Licor7500 (10 HZ)	CNR-1	Jan 2008 - Dec 2010	4520	Ma et al. (2011)
MY	40.6038N/ 117.3233E	Orchard	CSAT3,Licor7500 (10 HZ)	CNR-1	Jan 2008 - Dec 2010	350	Liu et al. (2013b)
DX	39.6213N/ 116.4270E	Crop	CSAT3,Licor7500 (10 HZ)	CNR-1	Jan 2008 - Dec 2010	100	Liu et al. (2013b)
GT	36.5150N/ 115.1274E	Crop	CSAT3,Licor7500 (10 HZ)	CNR-1	Jan 2008 - Dec 2010	30	Liu et al. (2013b)
YC	36.9500N/ 116.600E	Crop	CSAT3,Licor7500 (10 HZ)	CNR-1	Oct 2002 - Oct 2004	13	Flerchinger et al. (2009)
DT	31.5169N/ 121.9717E	Wetland	CSAT3,Licor7500 (10 HZ)	CNR-1	Jan 2005 - Dec 2007	5	Zhao et al. (2009)
SC	35.95N/ 104.133E	Dry land	CSAT3,Licor7500 (10 HZ)	CNR-1	Jan 2007 - Dec 2008	1965	Huang et al. (2008)
WS	36.6488N/ 116.0543E	Winter wheat / summer maize	CSAT3,Licor7500 (10 HZ)	CNR-1	Jan 2006 - Dec 2008	30	Lei and Yang (2010a)

1004

1005

1006

1007

1008

1009

Table 3. Comparison of accuracy of our flux data product and GLDAS against in-situ measurements from 11 Chinese flux towers. MB is mean of observation minus model simulation.

		Energy flux					Radiation flux				
		H (Wm^{-2})	LE (Wm^{-2})	G0 (Wm^{-2})	Rn (Wm^{-2})	**Mean**	SWD (Wm^{-2})	SWU (Wm^{-2})	LWD (Wm^{-2})	LWU (Wm^{-2})	**Mean**
Our flux data product	**Slope**	0.39	0.9	0.87	0.92	0.77	0.95	0.68	0.91	0.95	0.87
	Intercept	-0.5	-6.1	6.1	-20.2	-8.2	13.6	10.9	-0.66	16.6	9.9
	RMSE	21.5	21.9	11.7	36.2	22.8	28.3	10.2	32.8	9.6	20.2
	MB	14.7	10.1	-5.7	26.3	11.4	-5.7	-0.65	28.9	2.4	6.2
	R	0.41	0.85	0.50	0.86	0.66	0.89	0.78	0.98	0.99	0.91
	Sample	280	284	197	313	270	310	307	307	307	308
GLDAS	**Slope**	0.77	0.87	0.58	1.0	0.81	0.99	0.75	0.87	1.0	0.90
	Intercept	20.83	5.1	-1.34	8.0	8.2	34.9	13.1	27.7	-4.5	17.8
	RMSE	26.6	20.6	6.7	17.9	17.9	45.6	15.9	19.2	11.1	23.0
	MB	-15.8	0.75	3.0	-10.4	-5.6	-32.87	-4.6	13.5	-3.2	-6.8
	R	0.46	0.80	0.61	0.95	0.71	0.87	0.65	0.99	0.98	0.87
	Sample	249	250	162	281	236	275	272	272	275	274

Table 4. Comparison of statistical values reported in similar studies

Reference	Research area	Method	Statistical parameters	H (Wm^{-2})	LE (Wm^{-2})	Flux network	Note
This study	Chinese landmass	SEBS	RMSE	23.1	21.9	flux towers in China	
			MB	16.8	8.3		
			R	0.6	0.8		
Wang et al. 2007	Southern Great Plains, USA	Regression method	RMSE	×	29.8	flux towers in Southern Great Plains, USA	calculated from Table 9
			MB	×	12.17		
			R	×	0.91		
Jiménez et al. 2009	global	Statistical method	RMSE	×	×	AmeriFlux	calculated from Tables 5 and 7
			MB	-5.23	7.9		
			R	0.68	0.76		
Vinukollu et al. 2011b	global	SEBS	RMSE	40.5	26.1	AmeriFlux	calculated from Table 4
			MB	27.98	-7.74		
			R	0.53	0.51		

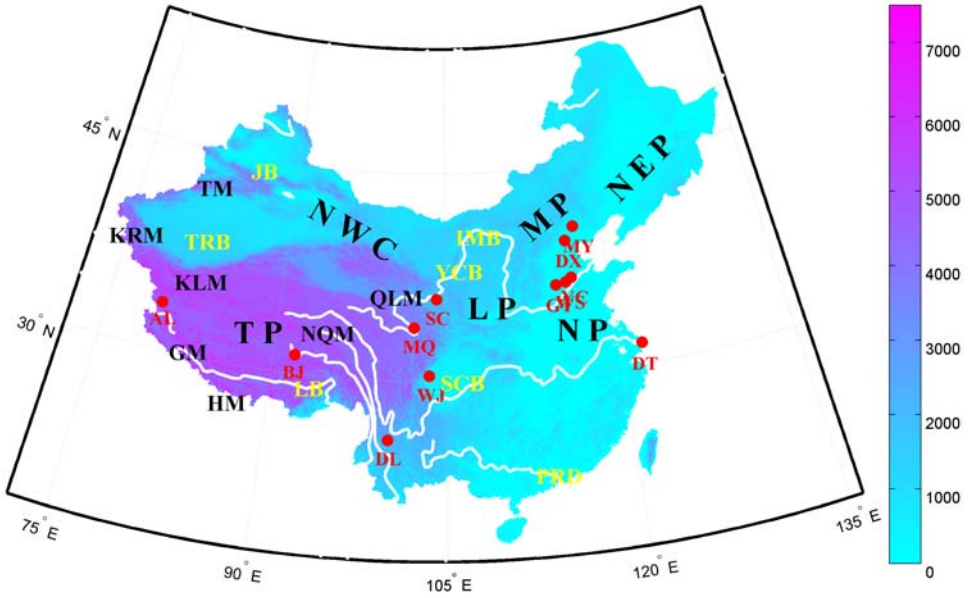

Figure 1. A DEM map of the Chinese landmass. The symbols indicate major physical phenomena: Tibetan Plateau (TP), northwestern China (NWC), inner Mongolian Plateau (MP), Loess Plateau (LP), North China Plain (NP), northeastern China Plain (NEP); Pearl River delta (PRD), Sichuan (SCB), Yinchuan (YCB), the inner Mongolian (IMB), and Lhasa (LB), Tarim (TRB), Junggar (JB) basins; the Himalaya (HM), Ganges (GM), Kunlun (KL), Karakorum (KRM), Tianshan (TM), Nyainqentanglha (NQM) and Qilian mountain (QLM) ranges. The plateau and plain letter symbols are in red type. The basins letter symbols are in green type. The flux station letter symbols are in yellow type. White lines show several of the major rivers in China.

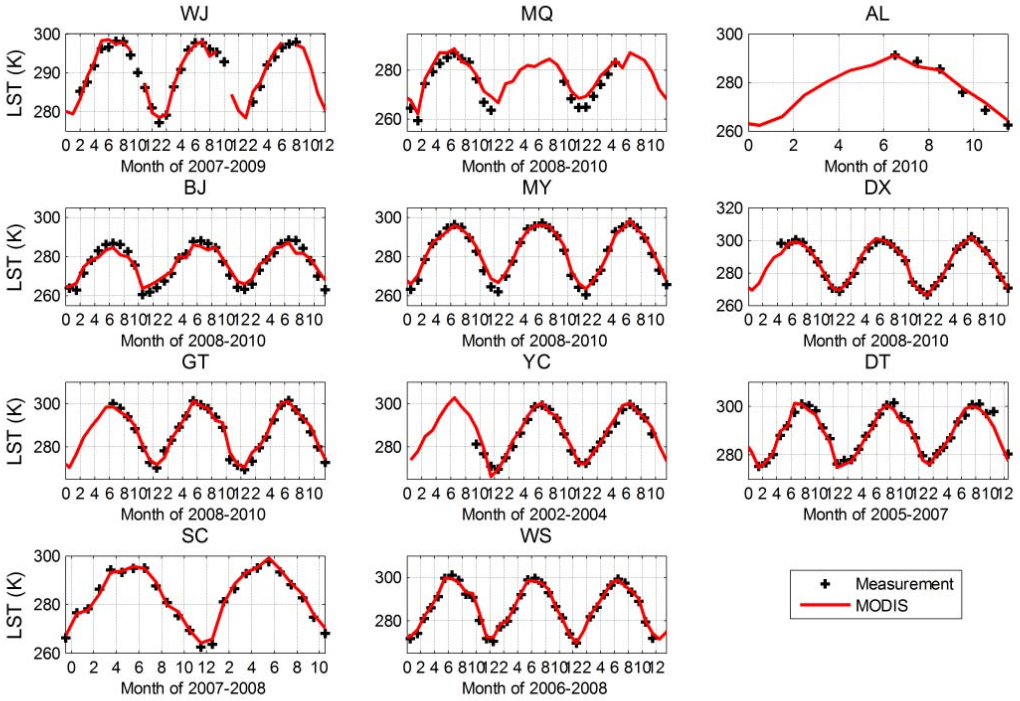

1054

1055 Fig. 2 Time series comparison of monthly averaged LST derived from MOD11C3&MYD11C3

1056 and in-situ measurements.

1057

1058

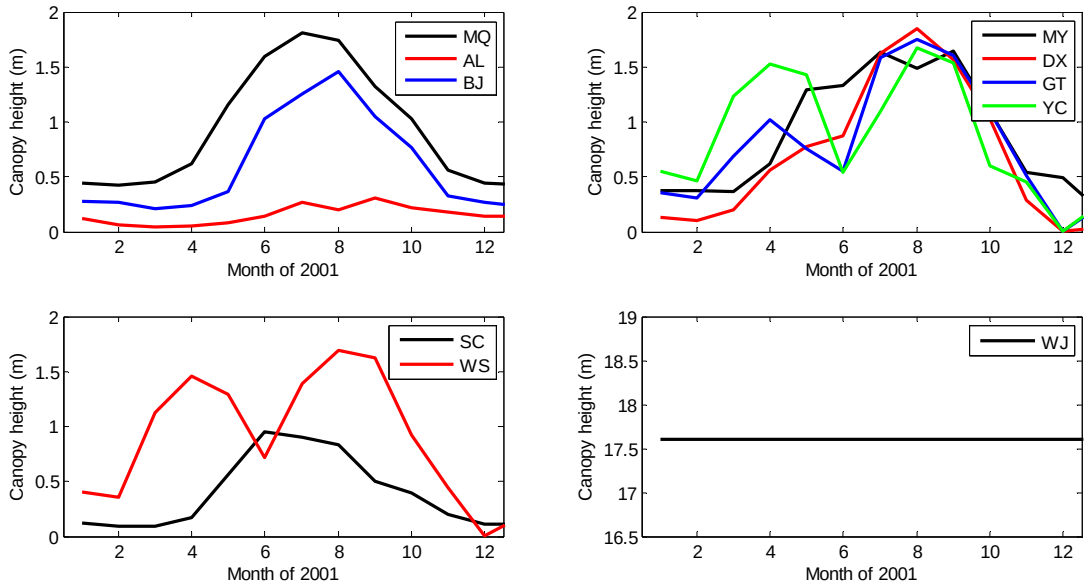

Fig. 3 Monthly variation of canopy height at the 10 flux stations

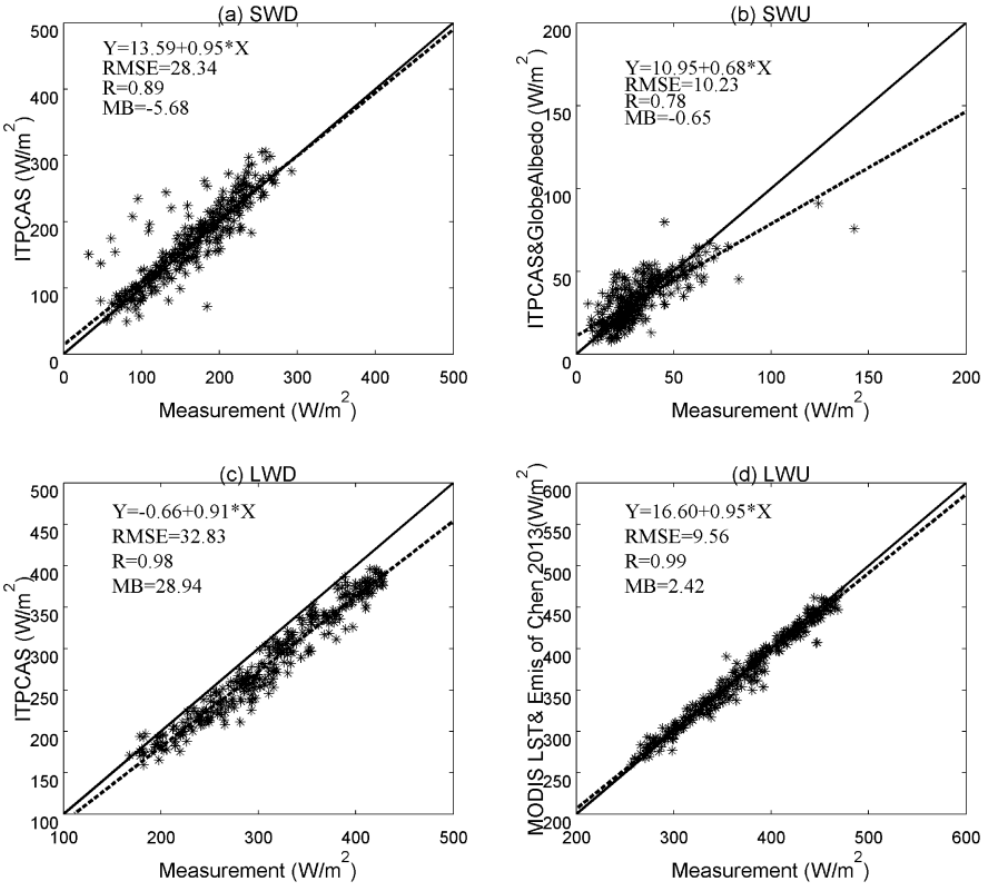

1067

1068 Figure 4 Scatter point for downward shortwave (SWD), upward shortwave (SWU) , downward
1069 longwave (LWD), and upward longwave (LWU) radiation against in-situ measurement.

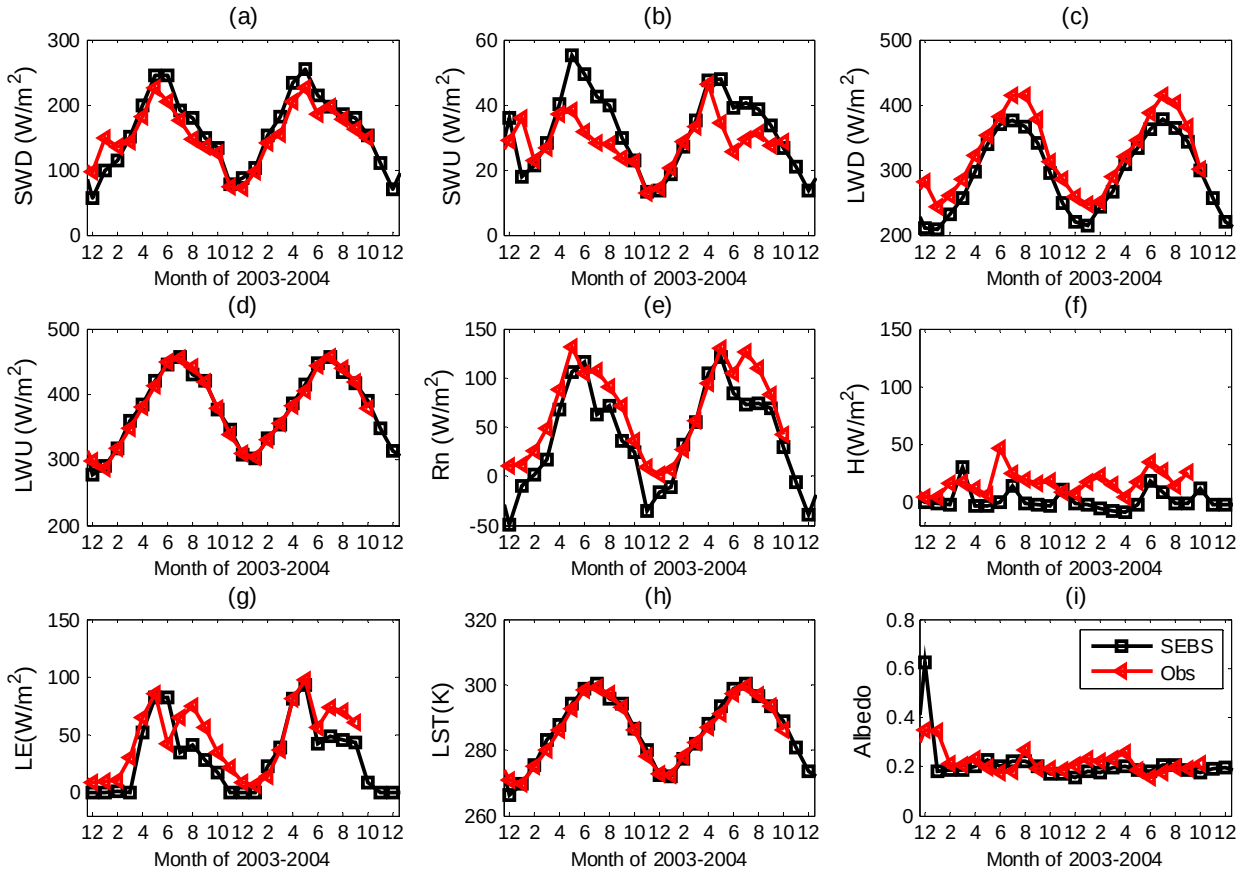

1070 Figure 5. Time-series comparison of SEBS input and output variables against measurements at
1071 Yucheng station**.** Black lines are SEBS results; red lines are measured values.

1072

1073

1074

1075

1076

1077

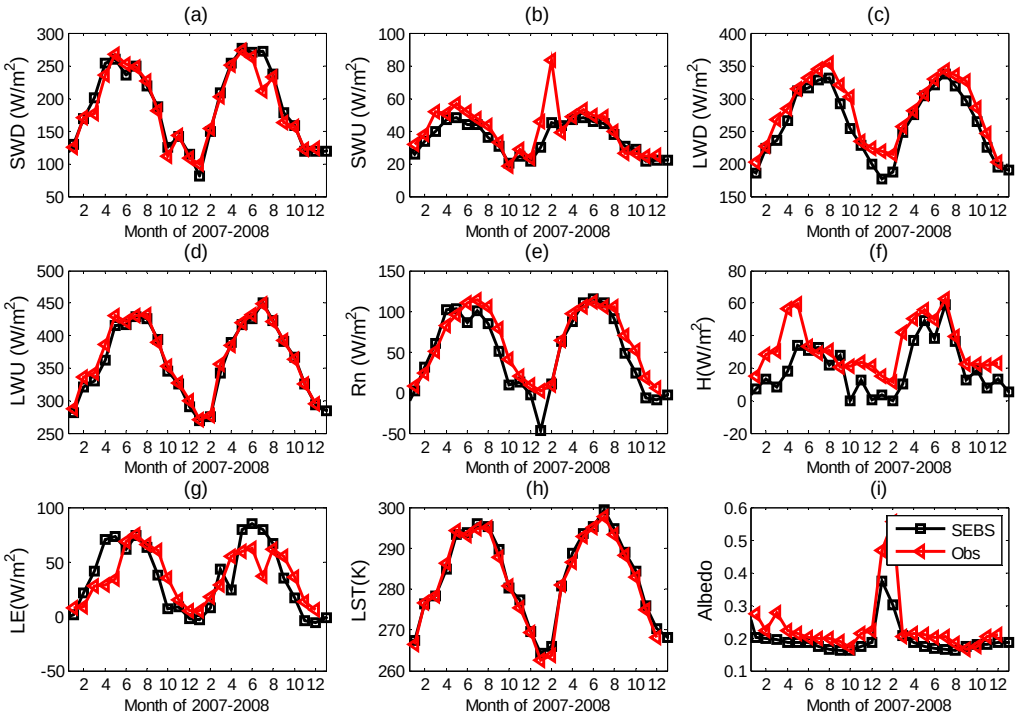

1078

1079 Figure 6. Time-series comparison of SEBS input and output variables against measurements at
1080 SC station. Black lines are SEBS results; red lines are measured values.

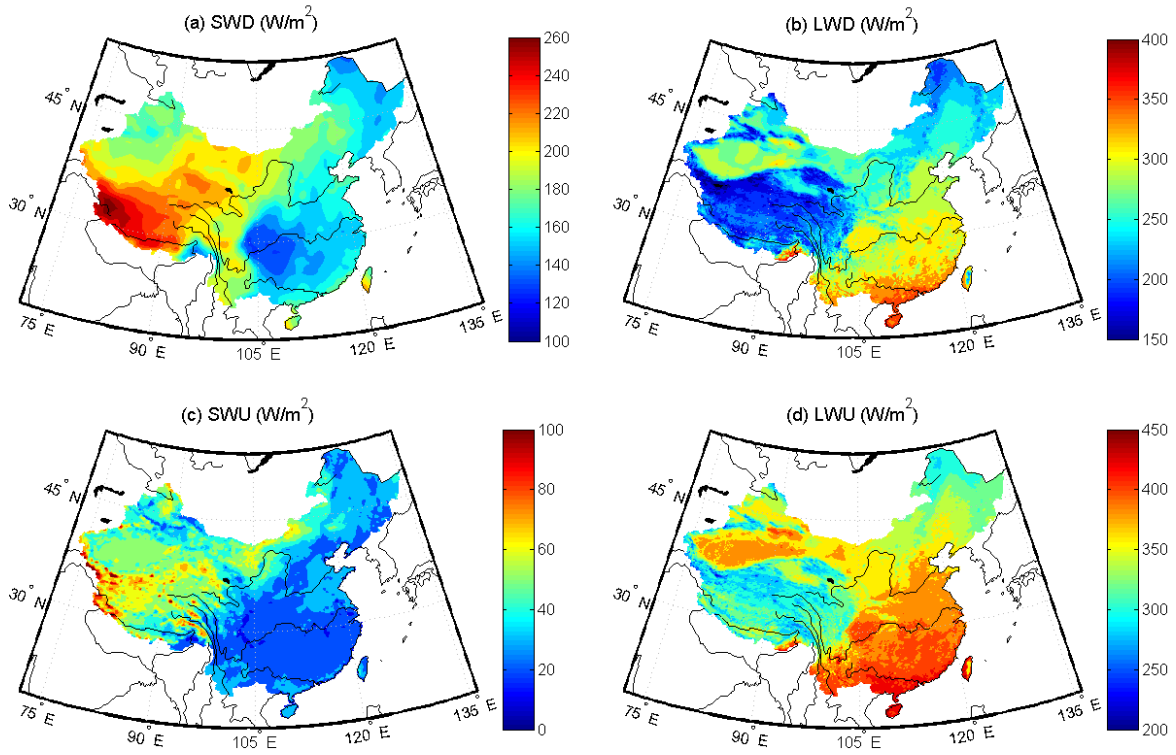

Figure 7. Maps of annual average (a) downward short-wave radiation (SWD), (b) downward long-wave radiation (LWD), (c) upward short-wave radiation (SWU), and (d) upward long-wave radiation (LWU) from 2001 to 2010. Black lines show several major rivers in China.

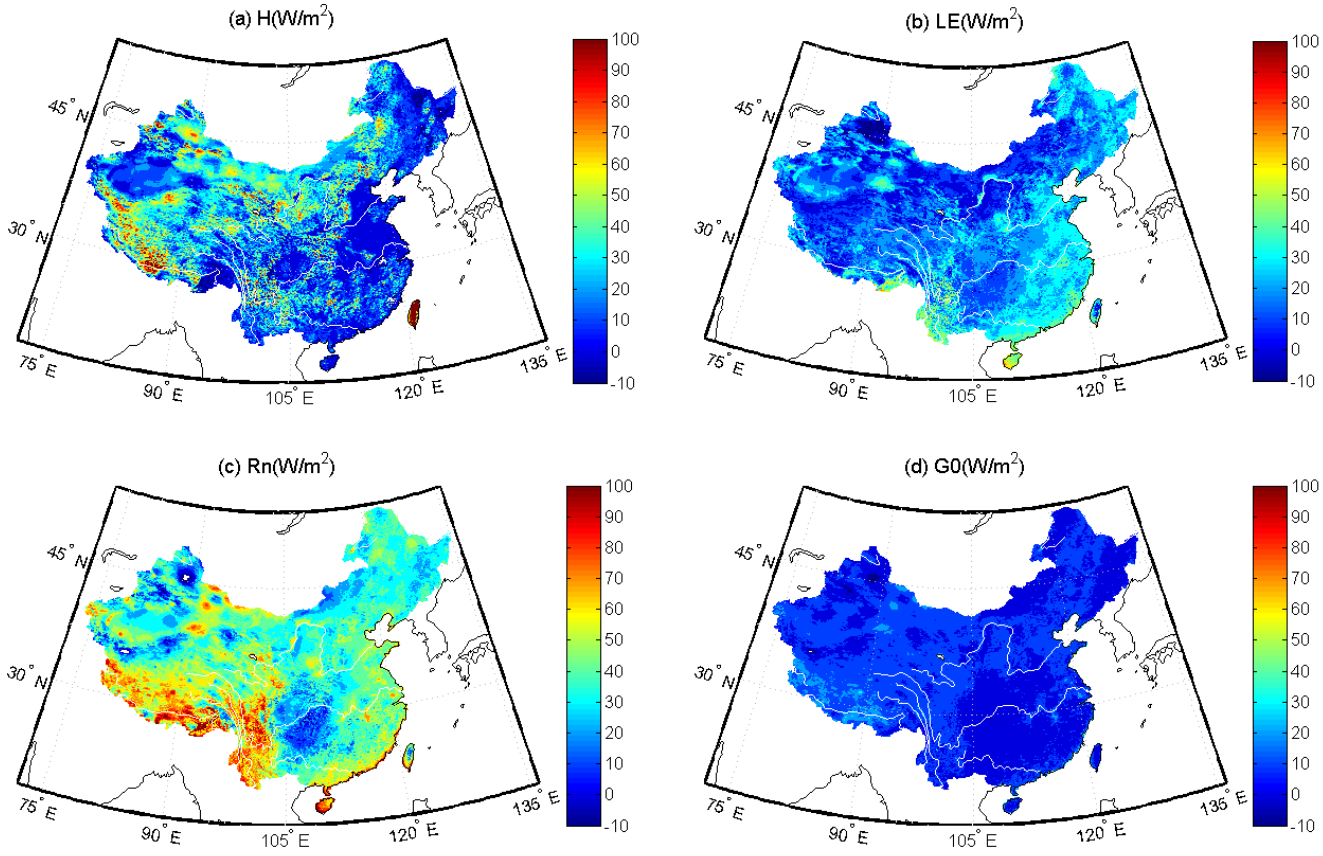

1089

1090 Figure 8. Maps of multiyear (2001–2010) means of retrieved fluxes: (a) sensible heat flux (H), (b)
1091 latent heat flux (LE), (c) net radiation (Rn), and (d) ground heat flux (G0). White lines show
1092 several major rivers in China.

1093

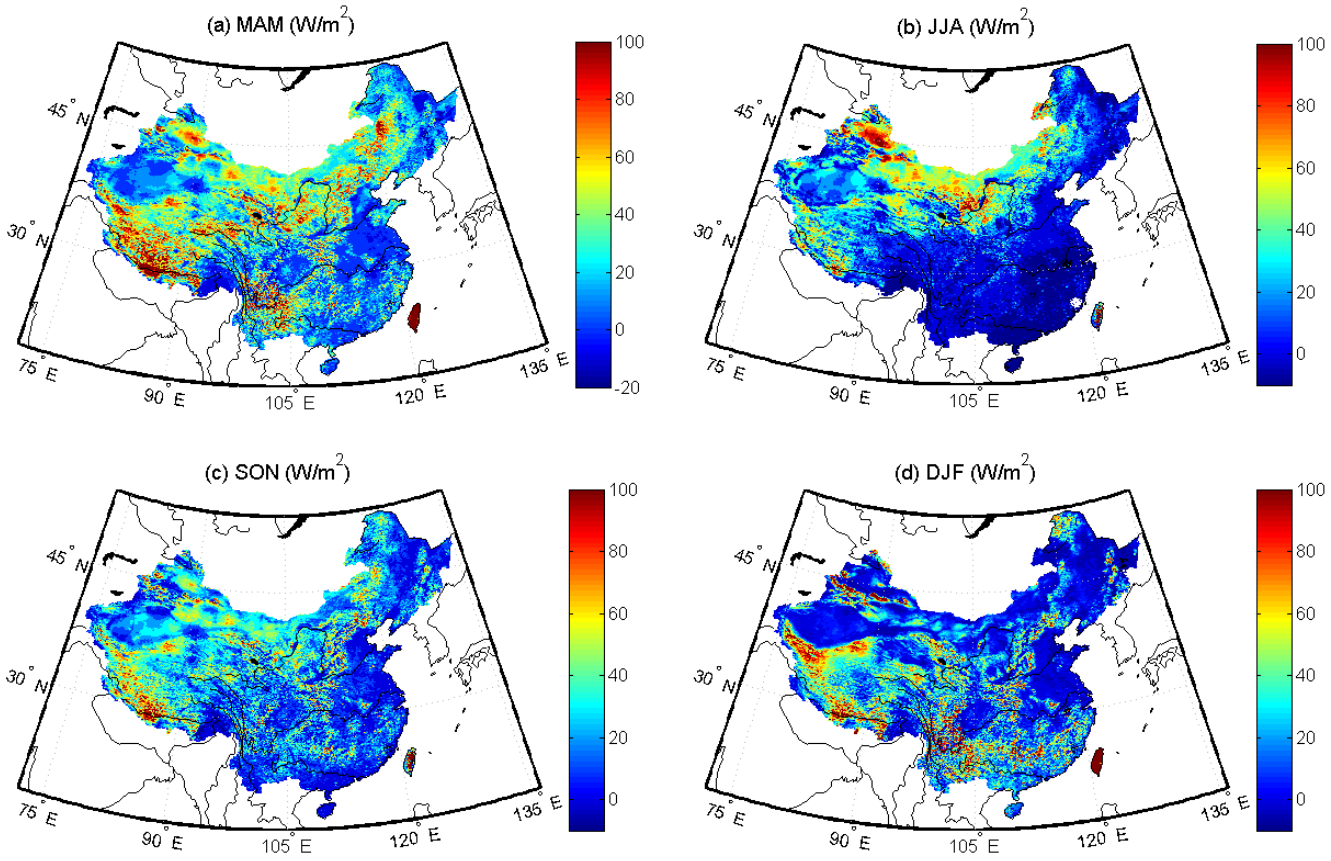

Figure 9. Maps of seasonal average sensible heat flux for (a) March-May (MAM), (b) June-August (JJA), (c) September-November (SON), and (d) December- February (DJF) from 2001 to 2010. Black lines show several major rivers in China.

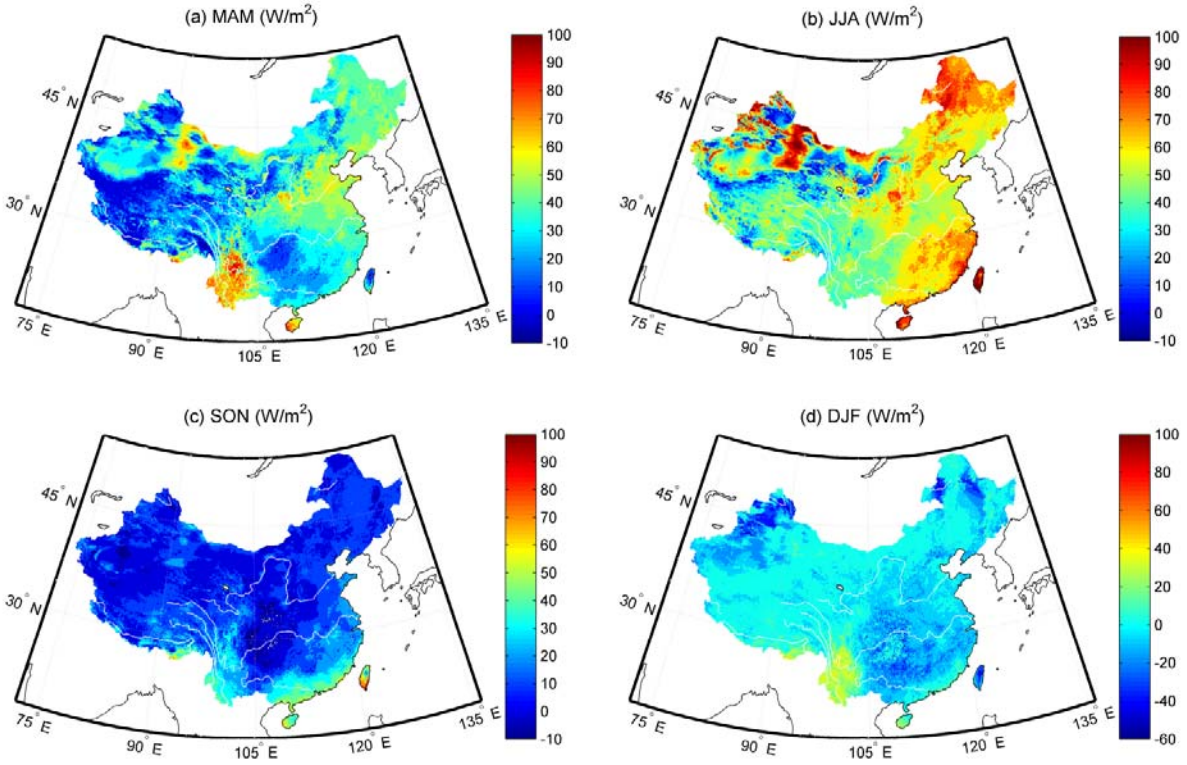

Figure 10. Maps of seasonal average latent heat flux for (a) March-May (MAM), (b) June-August (JJA), (c) September-November (SON), and (d) December- February (DJF) from 2001 to 2010. White lines show several major rivers in China.

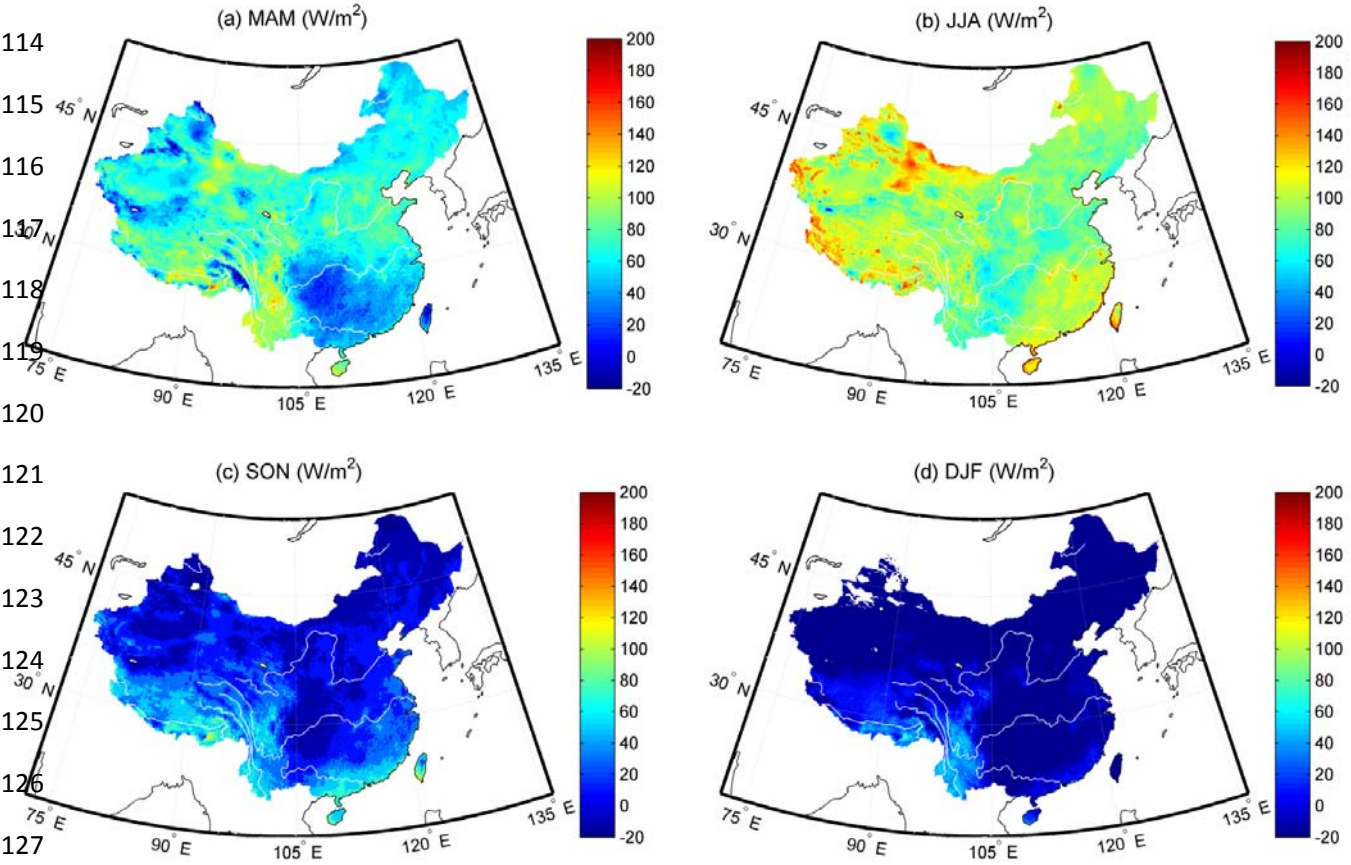

Figure 11. Maps of seasonal average net radiation for (a) March-May (MAM), (b) June-August (JJA), (c) September-November (SON), and (d) December- February (DJF) from 2001 to 2010. White lines show several major rivers in China.

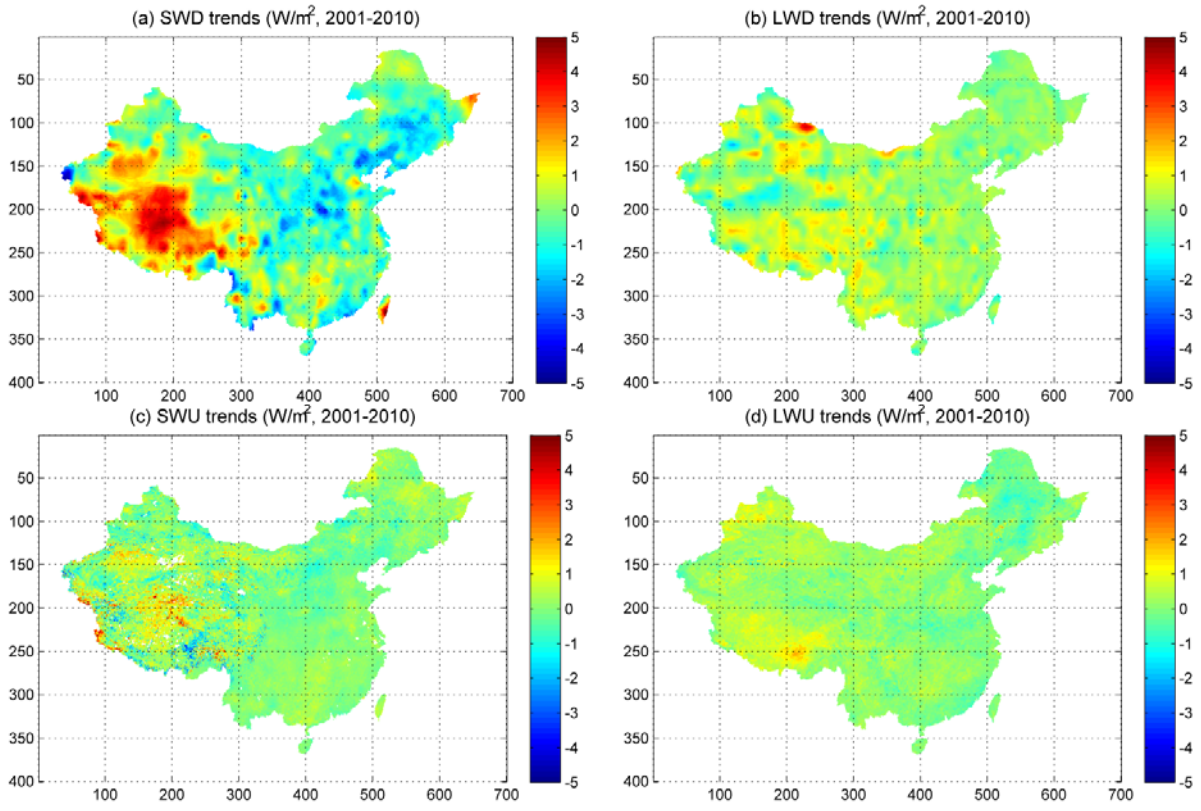

Figure 12. Spatial trends of (a) SWD (downward short-wave), (b) LWD (downward long-wave), (c) SWU (upward short-wave), and (d) LWU (upward long-wave radiation) for the Chinese landmass from 2001 to 2010.

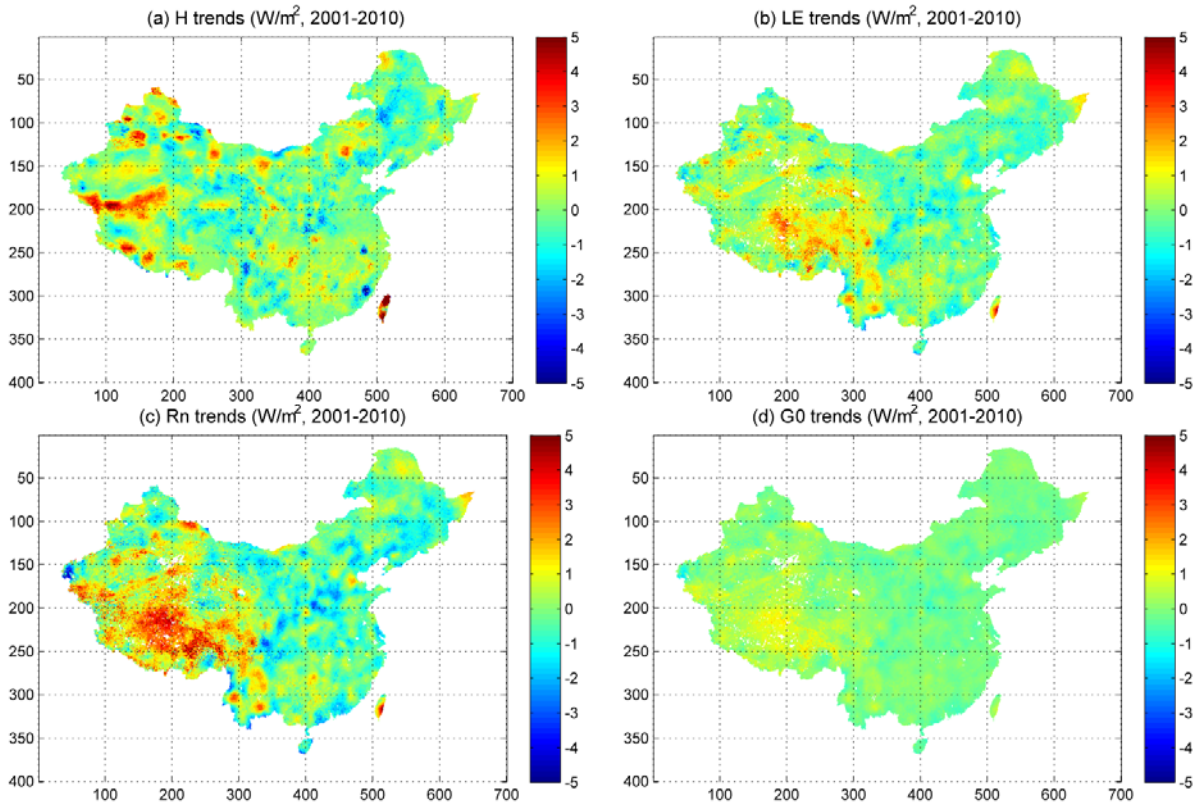

Figure 13. Spatial trends of (a) sensible heat flux (H), (b) latent heat flux (LE), (c) net radiation (Rn), and (d) ground heat flux (G0) on the Chinese landmass from 2001 to 2010.